THE DEVELOPMENT AND CHARACTERIZATION OF PIEZOELECTRIC-MAGNETOSTRICTIVE SMART SELF-SENSING COMPOSITES

By:

RELEBOHILE GEORGE QHOBOSHEANE

DISSERTATION

Submitted in partial fulfillment of the requirements

for the degree of Doctor of Philosophy at

The University of Texas at Arlington

May 2022

Supervising Committee:

Dr. Rassel Raihan (Advisor, Committee Chairman)

Dr. Kenneth Reifsnider (Co-Advisor)

Dr. Endel Iarve (Committee Member)

Dr. Ye Cao (Committee Member)

Dr. Ashfaq Adnan (Committee Member)

Acknowledgements

I want to thank my supervisor, Dr. Rassel Raihan, for supporting me academically, providing me opportunities to share my work, and aiding me to get to this point through the evolution of several projects. Thank you, Dr. Vamsee Vadlamudi, for assisting in my work and challenging me in my times at The University of Texas at Arlington throughout my research.

I would like to express my gratitude to Dr. Kenneth Reifsnider, Dr. Endel Iarve, Dr. Ashfaq Adnan and Dr. Ye Cao for their time and effort to serve on my committee. Their valuable inputs during comprehensive exam, and over the research has been of significant contribution to this dissertation.

I also want to thank to the Institute for Predictive Performance Methodologies (IPPM) at UTA Research Institute (UTARI) providing access to their facilities for all the experimentation and numerical work in my research.

I want to thank my family for their support during my studies at The University of Texas at Arlington. I especially would like to thank my parents, Paul and Matsepang Qhobosheane, for their gracious support of me financially and emotionally. Their guidance and encouragement have molded me into the person I am today, and I am forever grateful for them. Special thanks also go to my brother, Mapheelle Francis Qhobosheane, who dealt with my frustrations and was always available to listen. Finally, I want to thank the Fulbright Organization and the South African National Research Foundation for providing me with funding during my program.

Dedication

For my family.

Paul Mphahama, Mats'epang Bernice and Mapheelle Francis Qhobosheane.

Abstract

The composites industry is expanding due to growing global demand for high performance material. How do you ensure production of composites is as smooth and effective as possible while maintaining high quality of the material? The key issues in composites include crack occurrence, sticking to molds in the production process and durability differences during their operation. However, monitoring such cases can be challenging. The industry is in need of a smart solution to be able to obtain accurate data from the raw material. This work focuses on the development of smart composite materials. The word composite comes from the word composed which means made up from. The application of composite materials has spread out through numerous industries in recent years. Composite materials experience different deformations that lead to failure in different applications. These has led to the demand and development of various structural health monitoring (SHM) techniques. This also entails the development and application of a wireless magnetostrictive senor for SHM applications. Glass fiber reinforced polymer (GFRP) and carbon fiber reinforced polymer (CFRP) composites are selected in this work. The increasing demand of early detection of barely visible damage inside fiber reinforced polymer (FRP) composites has led to the development of advanced micro sensors capable of measuring local strains and defects within FRP composites. One of the major challenges in this type of local structural health monitoring (SHM) is the development of embedded sensors which can be safely placed into FRP composites while maintaining their high strength and light weight.

The characterization of mechanical properties of the developed smart self-sensing glass fiber composite is also another objective in this work. A composite sample with both magnetostrictive property and piezoelectric property is manufactured. The magnetostrictive property is achieved by the addition of Terfenol-D nanoparticles within the composite constituents and the piezoelectric

property by the addition of single-walled carbon nanotubes (SWCNTs). The presence of these foreign material within the composite system affects the overall composite mechanical properties. Composite prepreg samples of constant optimal nanoparticle volume fractions as per previous work are fabricated. Thermal properties will be investigated using deferential scanning calorimetry (DSC). Bonding properties in the presence of the nanoparticles will be characterized using Nicolet 6700 FTIR Fourier transform infrared (FTIR). Different mechanical tests will be performed to predict the smart self-sensing composite performance, coupled with statistical and FEA models to give in-depth understanding of these composites.

Table of Contents

List of Figures

Chapter 1: Introduction

1.1 Background

The development of smart self-sensing materials has been a topic of interest in recent years for most researchers. Promising strides have been made in both piezoelectric and magnetostrictive materials development. This work will contribute the development of smart materials with piezoelectric properties and magnetostrictive properties including advanced detection methods.

1.11 Piezoelectricity

The principle of piezoelectricity was discovered in the year 1880 by Pierre Curie and Jacques Curie [1]. They discovered that when a mechanical stress is applied on crystal structures of certain materials, electrical potential is generated across the material. This electrical potential was found to be proportional to the applied stress. This is the piezoelectric effect of the material. It was also found by Gabriel Lippmann in 1881 that applying electrical potential to these materials results in mechanical stress [2]. This phenomenon is said to be the inverse piezoelectric effect. The piezoelectric effect comes from molecular dipole moment within a material [3].

1.111 Molecular Dipole Moment

The molecular dipole moment of a material is dependent on the type of chemical bond its atoms has [4]. Chemical bond is the force that holds atoms together to form molecules and ionic compounds. Chemical bonds can be ionic or covalent bonds, which can be polar or non-polar. Non-polar are bonds formed between atoms with relatively equal electronegativity while polar covalent bonds are bonds between atoms with one with a high electronegativity than the other [5]. This creates an asymmetrical charge distribution that cause dipole moment. This happens when there is a charge imbalance in molecules as shown in Figure 1.

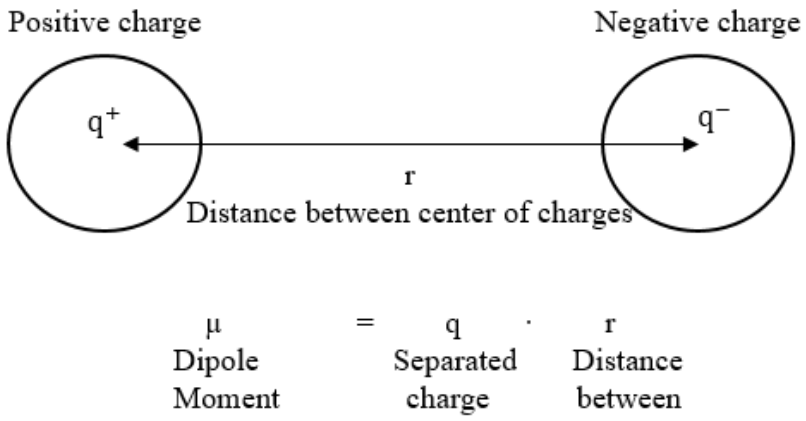

Figure 1. Chemical bonding dipole moments [5].

Figure 1 illustrates that a dipole is a set of 2 equal and opposite charge separated by some distance. In case of molecules, a dipole is created either due to charge separation or due to development of partial charges on bonded atoms [6]. Now, every dipole has a dipole moment and overall dipole moment of a molecule represents its polarity. The dipoles tend to have the same direction when next to each other therefore giving each dipole similar characteristic when next to each other [7]. This phenomenon can be observed in piezoelectric material during the piezoelectric effect.

1.12 Piezoelectric Effect

From molecular dipole moment, it is observed that each domain in a crystal has its own dipole moment, the crystal as a whole is non-polarized [8]. When a strong electrical filed is applied through the crystal, the domains orient themselves in the direction of the applied field [9]. During this orientation of domains, a mechanical stress will be generated. This is the process of inverse piezoelectric shown in Figure 2.

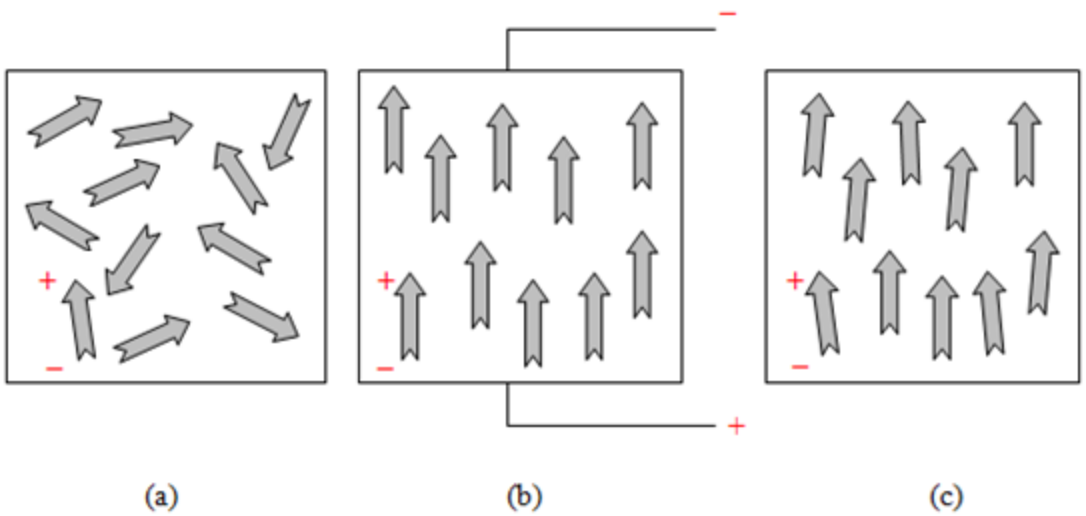

Figure 2. Shows electrical moments, a) before polarization, b) during polarization and c) after polarization [10].

The application of stress on these crystals results in the appearance of an electric potential across which is the direct piezoelectric effect [10]. The effect is explained by the displacement of ions in crystals that have a nonsymmetrical unit cell. When the crystal is compressed, the ions in each unit cell are displaced, causing the electric polarization of the unit cell [11]. Because of the regularity of crystalline structure, these effects accumulate, causing the appearance of an electric potential difference between certain faces of the crystal shown in Figure 3.

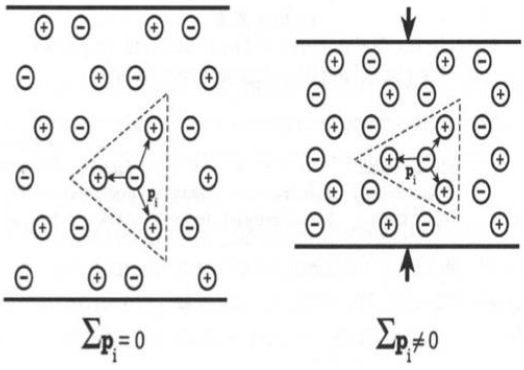

Figure 3. Two dimensional crystal piezoelectric effect [11].

A crystal possessing a center of symmetry cannot be piezoelectric because the dipoles within the primitive unit always cancel each other out [7]. In Figure 3, the net electrical dipole within the primitive unit of an ionic crystal lacking a center of symmetry does not vanish when external stress is applied. The piezoelectric principle is applied in the development of smart materials in this work with the magnetostrictive principle.

1.2 Magnetostrictive

The property of magnetostriction was discovered in 1842 by James Joule when observing a nickel specimen [12]. This property depends on the ability of a material to respond to a magnetic field, which is magnetism. It is based on the interaction of the magnetic moments in atoms [13]. The magnetic moments within a materials interaction lead to magnetism. This type of forces are non-contact and are in the form of dipoles with a repulsion property for similar poles and attraction property for unlike poles [14]. Materials with this property can be classified as partially oriented local atomic moment, which can be parallel or not parallel or randomly oriented local atomic moment couple, which is not coupled at all [14]. The alignment of the atomic moments either parallel or not parallel are a determining factor of either ferromagnetic, antiferromagnetic or ferrimagnetic materials. Ferromagnets are those materials that maintain a strong parallel coupling of their atomic moments in the absence of a magnetic field [15]. These materials exhibit magnetostrictive behavior and are due to the long range ordering of magnetic dipoles.

1.21 Ferromagnetism

Ferromagnetism is a magnetically ordered state of matter in which atomic magnetic moments are parallel to each other [15]. The phenomenon of ferromagnetism plays an important role in modern technologies. It is a physical basis for the creation of a variety of electrical and air-drying devices such as transformers, electromagnetic storage devices, hard drives devices and so on. This concept

can be observed in the electron configuration of a ferromagnetic material atom, take an example of iron [16]. Figure 4 shows the orbital diagram or iron, showing electrons in 3d orbital remain unpaired. Also we can see these 4 electrons spin in same direction. Each spinning electrons is a magnetic effect since it is rotation of electric charge. When electrons are paired, one electron spins in the opposite direction of other [17]. As a result there is no resultant magnetic effect. When the electrons are unpaired, the electronic magnetism becomes prominent. Such electrons are referred to as magnetization electrons.

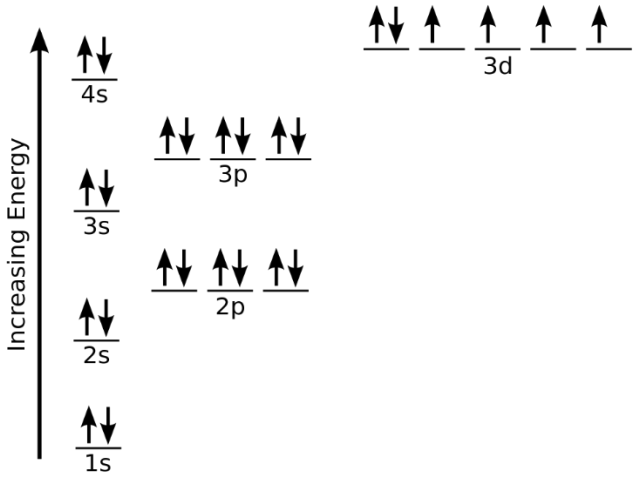

Figure 4. Iron electron configuration in orbital diagram [17].

In iron, there are four such unpaired electrons spinning in same direction. As a result, each iron atom gets the resulting magnetism [18]. Therefore each iron atom behaves as a magnetic dipole. Numbers of such magnetic dipole atoms align themselves in such a direction in the microscopic region shown in Figure 5 (a). These regions are called domain, as a result the domain itself has magnetic dipole behavior [16]. Now the question is: how are so many atomic dipoles aligned together in same direction in a domain although magnetization electrons of each atom of same domain spin in same direction? This is because other electrons which spin in the opposite direction

mainly in the fourth atomic shell interacted close range with the magnetization electrons. This interaction is attractive because of the attractive effect of their opposite spins.

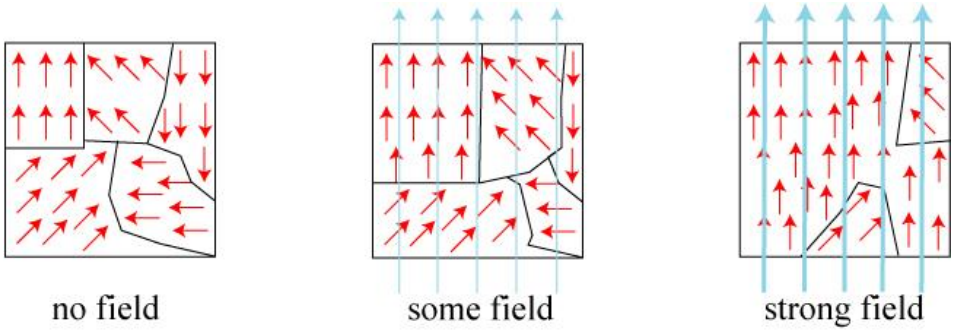

Figure 5. Iron ferromagnetic materials magnetization and filed direction [18].

These shell electrons influence the magnetization electrons of the iron atoms and align them in the same direction. These domains are randomly oriented in a piece of iron so there will be no net magnetization left behind [18]. If a magnetic field is applied to a piece of iron, the magnetic domains align themselves in the direction of applied magnetic field as shown in Figure 5. The piece of iron becomes magnetized. When the external magnetic field is removed, the iron piece remains magnetized to some extent. This behavior of iron is called ferromagnetism. The materials that exhibit this property are called ferromagnetic materials which include iron, cobalt and nickel or others.

1.22 Ferromagnetic Materials Magnetostriction

Ferromagnetic materials above Curie temperature are in their non-ordered magnetic state. Cooling these materials through their Curie temperature results in ordered magnetic moments over long range covering a large volume of atoms due to exchange interaction [19]. All moments lie parallel to each other in this volumes known as domains. The net magnetization throughout the material is zero due to the variation of spontaneous magnetization from domain to domain [18]. The initiation of ferromagnetism in an isotropic material in its paramagnetic state, when spontaneous

magnetization occurs leads to ordered magnetic moments. A strain (e) in the material is developed also known as a magnetostriction along a specific direction [20].

$$e(\theta) = e\cos^2\theta \tag{1.1}$$

where θ is the angle strains vary within each domain from the direction of spontaneous magnetization. Magnetostrictive materials entail polycrystalline grains with randomly oriented and any crystallographic direction [18]. The average deformation can be obtained by integration.

$$\lambda_0 = \int_{-\frac{\pi}{2}}^{\frac{\pi}{2}} e\cos^2\theta \sin\theta \, d\theta \tag{1.2}$$

Due to the presence of long range ordering of magnetic moments at the onset of ferromagnetism, this spontaneous magnetostriction is formed.

1.23 Field Induced Magnetostriction

The fractional change in length between magnetized and demagnetized material leading to magnetostriction defines the field-induced magnetostriction [15]. There is a transition from an ordered but demagnetized state to the ordered saturated state under the application of a magnetic field. In the saturated state, the magnetic moments in each domain are all aligned in the direction of the field therefore causing the strains to be parallel to the field. The resulting saturation magnetostriction can then be represented as the following [18],

$$\lambda_s = e - \lambda_0 = \left(e - \frac{e}{3}\right) = \frac{2}{3}e \tag{1.3}$$

The spontaneous strain within the material due to the magnetic ordering can be measured by measuring the saturation magnetostriction [18]. The saturation magnetostriction also depends on the angle to the magnetic field. For an isotropic material, the saturation magnetostriction $\lambda_s(\theta)$ at any angle θ to the field direction is given by,

$$\lambda_s(\theta) = \frac{3}{2}\lambda_s\left(\cos^2\theta - \frac{1}{3}\right) \quad (4)$$

where λ_s is the saturation magnetostriction along the direction of magnetization. The field is either applied parallel or perpendicular to a sample direction and their saturation magnetostriction is given in terms of the direction in which the field was applied as $\lambda_s||$ and $\lambda_s \perp$ for field applied in parallel and perpendicular directions to the selected sample direction, respectively [21]. The difference between these two quantities gives the spontaneous strain within a single domain.

$$\lambda_{s||} - \lambda_{s\perp} = \lambda_s + \frac{\lambda_s}{2} = \frac{3}{2}\lambda_s = e \quad (1.5)$$

1.24 Anisotropic Materials

The exchange interaction which occurs at the Curie temperature leads to spontaneous magnetization. However, it does not dictate in which direction the magnetization will align [15]. Therefore, magnetization is free to orient along any crystallographic direction without altering the internal energy. However, in all ferromagnetic materials there exists a preferred direction known as the "easy axis" in which the magnetization likes to align [22]. The direction varies for different classes of materials with different crystal structures but in general, rotation of the magnetization away from the easy direction increases the internal energy of the system. Since the energy of the system is at its minimum when the magnetization is aligned along the easy direction, rotation of the magnetization can only occur by means of a magnetic field [18]. This energy which dictates the preference in magnetization orientation is called the magnetic anisotropy, and the anisotropy that assigns energy to different directions in the crystal is called the magnetocrystalline anisotropy. Ferromagnetic materials magnetized to saturation state reach saturation magnetostriction as shown in Figure 6.

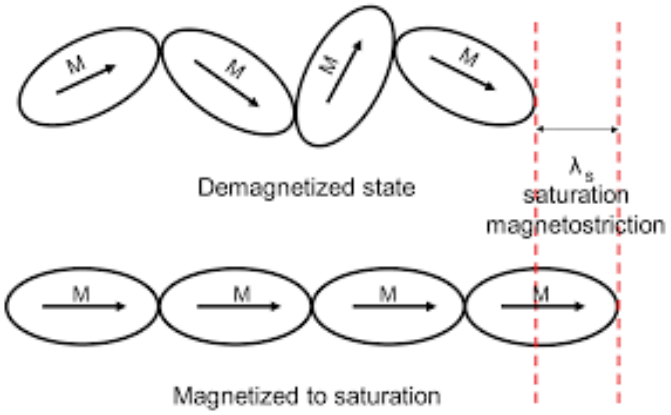

Figure 6. Magnetization of a ferromagnetic material to saturation magnetostriction [18].

Since most ferromagnetic materials exhibit some degree of anisotropy, the saturation magnetostriction needs to be defined relative to the crystal axes along which the magnetization lies. For a cubic crystal structure there are two principal directions in which the magnetization likes to orient: they are <100> or <111> crystallographic directions [23]. The directional dependence of the saturation magnetostriction of a single domain single crystal cubic structure is given by,

$$\lambda_s = \frac{3}{2}\lambda_{100}\left(\alpha_1^2\beta_1^2 + \alpha_2^2\beta_2^2 + \alpha_3^2\beta_3^2 - \frac{1}{3}\right) + 3\lambda_{111}(\alpha_1\alpha_2\beta_1\beta_2 + \alpha_2\alpha_3\beta_2\beta_3 + \alpha_3\alpha_1\beta_3\beta_1) \quad (1.6)$$

where λ_{100} is the saturation magnetostriction measure along the <100> direction, λ_{111} is the saturation magnetostriction along the <111> direction, $\alpha_1, \alpha_2, \alpha_3$ are directional cosines relative to the field direction of the axis along which the magnetic moments are saturated, and $\beta_1, \beta_2, \beta_3$ are the directional cosines relative to the field direction in which the saturation magnetostriction was measured [18]. The spontaneous strains along two principal axes are $e_{100} = (3/2)\lambda_{100}$ and $e_{111} = (3/2)\lambda_{111}$. Magnetostrictive effects arise due to the reorientation of magnetization by both magnetic fields and stress, and are known as magnetomechanical or magnetoelastic effect. Two

important ways of understanding ferromagnetism in metals are assuming that moments are localized to atoms and using the band structure of metals. Magnetostrictive materials are alloys of different ferromagnetic materials characterized by their magnetostrictive properties and other parameters as shown in Table I.

Table I. A preview of different magnetostrictive materials properties.

Magnetostrictive Material	**Magnetostriction (ppm)**	**Curie Temperature (^{0}C)**	**Density (ρ)**	**Magneto mechanical coupling coefficient (k)**	**Saturation Induction (B)**	**Elastic Modulus E (GPa)**
Metglas 2605SC	27	370	7.32	0.92	1.65	25-200
Metglas 2628MB	12	353	7.9	0.7	0.88	100-110
Terfenol-D	1500-2000	380	9.25	0.77	1.0	110
Piezoelectric (PZT)	20	325	7.6	0.66	1.2	52
Piezoelectric (PMN)	23	320	7.7	0.60	1.3	66
Polyvinylidene fluoride (PVDF)	18	360	1.7-1.8	0.90	1.35	1.5-2
Nitinol	12	300	0.233	0.67		83
Iron (Fe)	14	770	7.88		2.15	285
Nickel (Ni)	33	358	8.9	0.31	0.61	210
Cobalt (Co)	50	1120	8.9		1.79	210
50% Cobalt – 50% Iron	43	200	8.25	0.35	2.45	
50% Nickel – 50% Iron	27	500	8.75	0.36	1.60	
Terbium (Tb)	42	-48	8.33	0.34		55.7

$TbFe_2$	55	423	9.1	0.35	1.1	
Dysprosium (Dy)	32	-184	8.56			61.4
$Tb_{0.6}Dy_{0.4}$	15	385	7.8	0.47	1.2	61

The magnetostrictive material properties shown in Table 1 define the change length, curie temperature, density, coupling coefficient, saturation induction and elastic modulus for the material that determine its application in the sensor industry. Magnetostrictive sensor applications have extended to various applications in bio-engineering, aerospace, civil and other industries. These sensors can detect different parameters within a target specimen which include strain, temperature, force, torque, light intensity, current, voltage, magnetic field and electric field. For this to happen coupling of these properties is a necessity.

1.25 Magnetoelastic coupling

Magnetoelastic coupling is the interaction between the magnetization and the strain of a magnetic material [24]. It couples elastic, electric, magnetic and in some situations also thermal fields. This principle is of great industrial interest for use in sensors, actuators, adaptive or functional structures, robotics, transducers and MEMS [24]. A magnetostrictive material develops large mechanical deformations when subjected to an external magnetic field. This phenomenon is attributed to the rotations of small magnetic domains in the material, which are randomly oriented when the material is not exposed to a magnetic field. The orientation of these small domains by the imposition of the magnetic field creates a strain field [25]. As the intensity of the magnetic field is increased, more and more magnetic domains orientate themselves so that their principal axes of anisotropy are collinear with the magnetic field in each region and finally saturation is achieved. When an external force is exerted on a magnetic material, the lattice will be distorted

and therefore the magnetization orientation varied [25]. In the case of a cubic crystal, the energy density of a magnetoelastic coupling term is given as,

$$f = B_0\left(\varepsilon_{xx} + \varepsilon_{yy} + \varepsilon_{zz}\right) + B_1\left(\alpha_x^2\varepsilon_{xx} + \alpha_y^2\varepsilon_{yy} + \alpha_z^2\varepsilon_{zz}\right)$$

$$+2B_2\left(\sigma_x\sigma_y\varepsilon_{xy} + \sigma_y\sigma_z\varepsilon_{yz} + \sigma_z\sigma_x\varepsilon_{zx}\right) \quad (1.7)$$

Where B_0, B_1, B_2 are the magnetoelastic coupling constants, σ_i represents the direction cosines between the magnetization vector and the system coordinates and the strain components represented by ε_{ij} [26]. The coefficients of magnetoelastic coupling can be characterized by the change in area with strain of the magnetostrictive material and derived from the strain of the free energy [26].

$$B_{ij} = \frac{1}{\alpha_i\alpha_i}\frac{\partial f}{\partial \varepsilon_{ij}} \quad (1.8)$$

If the magnetostrictive strain depends on the rotation of the magnetization vector, then a general result can be obtained by assuming $\frac{\partial f}{\partial \varepsilon_{ij}} = 0$.

$$e(B) = \left(\frac{B}{3E}\right)\left(4m^2(H)\right) - 1 \quad (1.9)$$

Where B still represents the magnetostriction coupling coefficient and using the integrated formulation of the Maxwell and Gibbs-Duhem [25] thermodynamic relationship of free energy, the result can be given as,

$$-\frac{B}{3}\left[\frac{4m^2(H) - 1}{E(H)} - \frac{4m^2(0) - 1}{E(0)}\right] = \int_0^m \frac{\mu_0 Ms}{E}\left(\frac{\partial H}{\partial e}\right)_\sigma dm \quad (1.10)$$

When the changes in elastic constants are neglected due to the applied strain being much greater and defining the area difference between the magnetization and field loops as $\Delta A = \int_0^m \left(\frac{\partial H}{\partial e}\right)_\sigma dm$ [22] then,

$$B = -\frac{\mu_0 M_s \Delta A}{(1+v)[m^2(H) - m^2(0)]} \tag{1.11}$$

1.3 Problem Statement

This work focuses on the development and application of a wireless magnetostrictive, piezoelectric smart material for SHM applications. Glass fiber reinforced polymer (GFRP) and carbon fiber reinforced polymer (CFRP) composites are selected in this work. The increasing demand of early detection of barely visible damage inside composites has led to the development of advanced micro sensors capable of measuring local strains and defects within FRP composites. One of the major challenges in this type of local structural health monitoring (SHM) is the development of embedded sensors which can be safely placed into FRP composites while maintaining their high strength and light weight.

A review of magnetostrictive sensors based on different magnetostrictive effects is carried out in this work. The dependence of these sensors on the magnetic field, coupling and detection method has been emphasized through different works. There are multiple limitations with magnetostrictive sensor devices currently under development. The strength of the excitation is one of the main limitations in magnetostrictive sensors. The excitation signal depends on the design of the excitation coil for the generation of guided waves. This drawback affects the size of the device and the distance of the excitation from the target sample. Improvement in this area would contribute to the wireless factor of this type of sensors. Magnetostriction sensors are very sensitive to their environment such as the interaction between the change in magnetic field of the earth and the

magnetic components of the system which may induce soft iron bias magnetic field. The magnetized components of the system may also result in hard iron bias. A solution for this potential issue is of importance, especially for sensors used on aircrafts to avoid potential interaction of magnetic fields with aircraft magnetometers. The working principles of magnetostriction sensors depends on numerous parameters that are affected by a slight change in the other. For instance, the magnetic field and guide wave propagation is affected by the angle of the magnet itself. A slight change in the angle may affect the guided waves to the target sample. This therefore affects the precision of these devices. The sensors are made of metal alloys, which do not have good bonding properties with target materials such as composites and this leads to generation of damage precursors. The need for bond improvement methods of magnetostrictive alloys with target material is one of the major gap. Another gap is the need for sensor validation methods in this new sensing techniques. Some studies validate the accuracy of the magnetostrictive sensor data by comparison studies with other sensors such as electromagnetic sensors, acoustic sensors and others.

Reduction of these limitations with novel contributions to the development of magnetostrictive sensors would have a high impact to this research. Potential areas of improved from current developments were noted. In recent years, strides have been made in the development of the testing setup to improve the quality of the collected signal even though there is still a lot to be done compared to other SHM sensors currently in industry. These types of sensors have a potential to replace current structural health monitoring sensors due to their potential wireless capability and real time SHM.

1.4 Objectives

- The aim of this research work is to develop piezoelectric magnetostrictive smart composites with advanced sensing capability. The composite piezoelectric property will be achieved from the dispersion of single walled carbon nanotubes (SWCNTs) and the magnetostrictive property from Terfenol-D nanoparticles and a wireless detection method will be developed to sense the response.
- Finite element analysis (FEA) will be used to examine the feasibility of modeling the piezoelectric (change in electric field) and magnetostrictive (change in magnetic field) self-sensing responses in the presence of applied stress. The numerical work will be coupled with a series of mechanical tests to characterize the piezoelectric response, magnetostriction response and mechanical strength. Tensile tests of the composite samples manufactured as is (virgin), samples with SWCNTs, with Terfenol-D nanoparticles and with both SWCNTs and Terfenol-D nanoparticles will be conducted.
- Smart self-sensing composite performance prediction: Thermal properties will be investigated using deferential scanning calorimetry (DSC). The aim is to characterize the curing properties of the prepreg samples with different nanoparticles before fabrication of the composite samples to explore the effect of the nanoparticles on the manufacturing properties. Bonding properties in the presence of the nanoparticles will be characterized using Nicolet 6700 FTIR Fourier transform infrared (FTIR). Several spots will be targeted on the prepreg substrates coated with SWCNTs and Terfenol-D to determine FTIR absorption peaks. The samples fabricated as per ASTM standards will then be passed through a series of mechanical tests to explore both mode I and mode II fracture toughness. The aim is to investigate the effect of nanoparticles on the composite delamination properties.

1.5 Dissertation Outline

This research work focuses on the development of a piezoelectric magnetostrictive smart composite with advanced sensing capability. The composite piezoelectric property is achieved from the dispersion of single walled carbon nanotubes (SWCNTs) and the magnetostrictive property from Terfenol-D nanoparticles. Finite element analysis (FEA) is used to examine the feasibility of modelling the piezoelectric (change in electric field) and magnetostrictive (change in magnetic field) self-sensing responses in the presence of applied stress. The numerical work was coupled with a series of mechanical tests to characterize the piezoelectric response, magnetostriction response and mechanical strength. All this will be developed in a series of tasks to the completion of this research.

Chapter 2 unpacks current studies on magnenetostrive sensors and illustrates the development of the sensor system to be used in this work for the detection of magnetostrictive composites. Composites specimen with magnetostrictive materials are developed in this work to demonstrate the working of the developed sensor.

Chapter 3 focuses on the fabrication of smart self-sensing composite with piezoelectric and magnetostrictive properties. Preliminary FEA modeling and experimental characterization using wireless detection systems will be done.

Chapter 4 focuses on this task will be on performance prediction of the smart self-sensing composite samples. A composite sample with both magnetostrictive property and piezoelectric property is manufactured. The magnetostrictive property is achieved by the addition of Terfenol-D nanoparticles within the composite constituents and the piezoelectric property by the addition of single-walled carbon nanotubes (SWCNTs). The samples fabricated as per ASTM standards were then passed through a series of mechanical tests to explore both mode I and mode II fracture

toughness. The aim was to investigate the effect of nanoparticles on the composite delamination properties and inter-laminar fracture toughness.

Chapter 5, Here the detected sensor data and detected defects are correlated with the damage modes developed within the fabricated smart self-sensing composite samples.

1.6 References

[1] Athenstaedt, Herbert. "PYROELECTRIC AND PIEZOELECTRIC PROPERTIES OF VERTEBRATES." https://doi.org/10.1111/j.1749-6632.1974.tb26780.x (1974).

[2] Bozorth, R. M. and Walker, J. G. "Magnetostriction of Single Crystals of Cobalt and Nickel Ferrites." American Physical Society 88.5 (1952): 1209.

[3] Callen, Earl. "Magnetostriction." Journal of Applied Physics 39.2 (2008).

[4] D. Vatansever, E. Siores and T. Shah. "Alternative Resources for Renewable Energy: Piezoelectric and Photovoltaic Smart Structures." DOI: 10.5772/50570 (September 19th 2012).

[5] Daehee Seol, Bora Kim and Yunseok Kim. "Non-piezoelectric effects in piezoresponse force microscopy." Current Applied Physics 17.5 (2017): 661-674.

[6] Domann, John Patrick. "On Magnetoelastodynamics." https://escholarship.org/uc/item/431786px (2016).

[7] Ederer, Daniel Fritsch and Claude. "First-principles calculation of magnetoelastic coefficients and magnetostriction in the spinel ferrites CoFe." PHYSICAL REVIEW B 86.014406 (July 2012).

[8] Furukawa, T. "Piezoelectricity and pyroelectricity in polymers." IEEE Transactions on Electrical Insulation 24.3 (June 1989): 375-394.

[9] Hall, R. C. "Single Crystal Anisotropy and Magnetostriction Constants of Several Ferromagnetic Materials Including Alloys of NiFe, SiFe, AlFe, CoNi, and CoFe." Journal of Applied Physics 30.https://doi.org/10.1063/1.1735247 (2004).

[10] Hathaway, K., & Clark, A. "Magnetostrictive Materials." MRS Bulletin 18.doi:10.1557/S0883769400037337 (n.d.): 34-41.

[11] Hossein Bisheh, Nan Wu and David Hui. "Polarization effects on wave propagation characteristics of piezoelectric coupled laminated fiber-reinforced composite cylindrical

shells." International Journal of Mechanical Sciences 161-162.https://doi.org/10.1016/j.ijmecsci.2019.105028 (2019).

[12] Jin Zhang, Chengyuan Wang and Chris Bowen. "Piezoelectric effects and electromechanical theories at the nanoscale." Nanoscale 22 (2014).

[13] Lee, E W. "Magnetostriction and Magnetomechanical Effects." Reports on Progress in Physics 18.184 (1955).

[14] M. A. Migliorato, J. Pal, R. Garg, G. Tse, H. Y.S. Al-Zahrani, and U. Monteverde. "A review of non linear piezoelectricity in semiconductors." AIP Conference Proceedings 32.https://doi.org/10.1063/1.4870192 (2014).

[15] M. V. Matyunina, M. A. Zagrebin, V. V. Sokolovskiy, O. O. Pavlukhina,V. D. Buchelnikov, ,A. M. Balagurov & I. S. Golovin. "Phase diagram of magnetostrictive Fe-Ga alloys: insights from theory and experiment." Phase Transitions: A Multinational Journal 92.2 (2018): 101-116.

[16] Marcelo J. Dapino, Ralph C. Smith. "A MAGNETOELASTIC MODEL FOR VILLARI-EFFECT MAGNETOSTRICTIVE SENSORS." Journal of Intelligent Material Systems and Structures DOI: 10.1177/1045389X02013011005 (n.d.).

[17] Martin, Richard M. "Piezoelectricity." PHYSICAL REVIEW B 5.4 (1972): 1607-1613.

[18] Mason, W. P. "A Phenomenological Derivation of the First- and Second-Order Magnetostriction and Morphic Effects for a Nickel Crystal." PHYSICAL REVIEW JOURNALS ARCHIVE 82 (1951).

[19] Ounaies, J. S. Harrison Z. "Piezoelectric Polymers." 3. https://doi.org/10.1002/0471440264.pst427 (15 July 2002).

[20] panelGöranEngdahl, Author links open overlay. "Chapter 1 - Physics of Giant Magnetostriction." Handbook of Giant Magnetostrictive Materials. https://doi.org/10.1016/B978-012238640-4/50017-6, n.d. 1-125.

[21] panelN.C.KoonC.M.WilliamsB.N.Das, Author links open overlay. "Giant magnetostriction materials." Journal of Magnetism and Magnetic Materials 100.1-3 (1991): 173-185.

[22] Peng Bai, Guang Zhu, Yu Sheng Zhou, Sihong Wang, Jusheng Ma, Gong Zhang & Zhong Lin Wang. "Dipole-moment-induced effect on contact electrification for triboelectric

nanogenerators." Nano Research 7.https://doi.org/10.1007/s12274-014-0461-8 (2014): 990-997.

[23] R. M. Bozorth, Elizabeth F. Tilden, and Albert J. Williams. "Anisotropy and Magnetostriction of Some Ferrites." PHYSICAL REVIEW JOURNALS ARCHIVE 99 (1955).

[24] Shigeyasu Ito, Koichi Aso, Yoshimi Makino, and Satoru Uedaira. "Magnetostriction and magnetization of iron-based amorphous alloys." Applied Physics Letters 37.https://doi.org/10.1063/1.92029 (2008).

[25] Somkun, Sakda, et al. "Magnetostriction Anisotropy and Rotational Magnetostriction of a Nonoriented Electrical Steel." IEEE Transactions on Magnetics 46.2 (Feb. 2010): 302-305.

[26] Uchino, K. "The Development of Piezoelectric Materials and the New Perspective." Advanced Piezoelectric Materials ISBN 9780081021354 (2017): 1-92.

Chapter 2: The Development of a Magnetostrictive Strain Sensor

2.1 Introduction

The development of magnetostrictive sensors has shown substantial improvements in recent years. More researchers have put focus on applications in structural health monitoring (SHM) for various applications including engineering and biological applications. In biological studies, the ability of magnetostrictive materials to change mechanical behavior in the presence of a magnetic field has made way for different sensing avenues. This includes studies on cell behavior analysis, organ monitoring systems and bones health monitoring. The sensitivity of magnetostrictive materials to the change in strains contributing to Villari effect is used within the human body for these sensing applications. This property was used in [27] to explore osteomalacia caused by deficiency of vitamin D in bones. Osteomalacia causes bones to weaken and soften up. The presence of a magnetostrictive sensor within the bone structure proved to sense very low pressure changes on the bone due to osteomalacia [27]. Coating magnetostrictive materials with highly temperature sensitive materials enabled temperature sensing applications within the human body. Numerous studies have showed need to meet biocompatibility standards leading to the modification of magnetostrictive material composites composition. This work focuses on the structural health monitoring applications of magnetostrictive sensors.

Damage detection in different structures due to changes in environmental factors has been a topic of interest for years. The use of magnetostrictive materials to develop wireless sensors has therefore peaked the interest of most researchers. Studies such as [28] from a research group at the University of Sheffield have proved the working of magnetostrictive materials in damage detection for structural health monitoring applications. This was a numerical modeling study which entailed polymer composites with both embedded and surface placed magnetostrictive materials. The

ferromagnetic magnetostrictive material change in shape during different types of loads resulted in the change in magnetization around the composite. This study showed that magnetostrictive ribbons placed on the surface of the composite would peel off during loading while embedded magnetostrictive ribbons could deform with the composite through its loading journey. A wireless detection method was used to illustrate how damages within the composite could be detected using magnetostrictive ribbons and detection energy levels explored. This, amongst other works has proved the working of magnetostrictive material sensors for structural health monitoring applications. The development of strain sensors using magnetostrictive materials for SHM applications has spread through different industries. Magnetostriction is a transduction process in which electrical energy is converted to mechanical energy. As magnetostrictive materials exhibit a change in dimension when placed in a magnetic field, magnetostriction inverse generates guided waves that could be used in strain sensing applications.

2.11 Working Principle

The working principle of Villari effect sensors is demonstrated below. The modified magnetostrictive material is placed within a targeted composite material for detection and two coils, pickup and detection close to the surface material. The supplied excitation voltage is changed by the magnetostrictive material between the composite as it goes through different deformations and change in magnetic field pickup by the second coil [29]. This principle is shown in Figure 7 below.

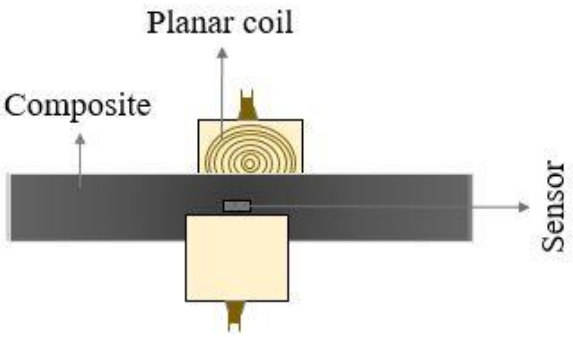

Figure 7. Villari effect within the composite material.

2.12 Magnetostrictive Sensors Applications

Work using the magnetostrictive guided waves to detect defects in in hollow cylindrical structures as well as plate and plate-like structures was done by Joseph L. Rose [28]. A magnetostrictive material requires the presence of a magnetic field, excitation and pickup coils. Joseph's work consisted of an array of exciting coils to generate controlled guided waves and similar array of pickup coils which were within proximity to the surface of the magnetostrictive material. For SHM of circular structures, the position of the magnets and location of the poles were the main factors. Each of the magnets were arranged such that as one circles the magnetostrictive material in a clockwise direction, the north pole of a magnet was encountered first, and the south pole of the magnet encountered second [28]. Once the bias magnetic field was induced, the magnets could be removed and detection of reflected guided waves for SHM continued.

The covered detection area range using magnetostrictive sensors has been a limitation in most works. Different methods have been developed to overcome this which include the fabrication of composite materials with magnetostrictive materials in their composition. In 2016, a group from University of Wisconsin-Milwaukee [30] developed a composite structure of Terfenol-D particles, epoxy and aluminum substrates. The composite samples were subjected to loading stresses to

monitor the structured health during the application of stresses. The behavior of the sensor was gathered from the magnetic susceptibility which depended on inductance (L) [30].

$$L = \frac{N^2 \mu_0 t}{l_g}(h\chi_m + a) + L_s \tag{2.1}$$

where N is the number of turns the high permeability coil and core that was designed to extract values of the susceptibility by measuring inductance [30]. μ_0 is the permeability of free space, L_s is the series inductance caused by the core and air gaps between the core and the composite, a is the thickness of the core at its air gap, and l_g and t are the composite dimensions [30]. This work [30] demonstrated that composites containing magnetostrictive material depend highly on the volume fraction and magnetostrictive particle orientation for improved magnetostriction which in turn affects the Villari effect. Application of magnetostriction materials for SHM can also be done by embedding the material within the composite. This is demonstrated by Oliver J. Myers's [31] work on polymer composites embedded with Terfenol-D particles. This work focuses on the coupling of the mechanical stress applied on the composite sample during loadings with the magnetic properties of the magnetostrictive material for the characterization of the sensor. Similar, the testing setup in this work too entailed two coils, pickup and excitation with the composite sample between in the presence of a bias magnetic field as shown in Figure 8 [31].

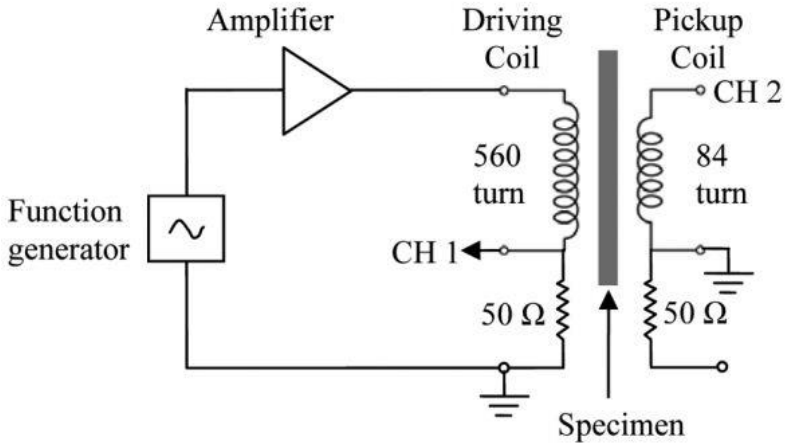

Figure 8. Villari effect detection using a pick up and excitation coil [5].

The application of stress to the composite samples embedded with Terfenol-D particles resulted in an increase in voltage response therefore demonstrating the detection of the Villari effect which could be related to the composite defects [31]. The main issue demonstrated is this work was the counter action of the addition of the magnetostrictive nanoparticles within the composite for SHM, as their presence as foreign material within the composite affected its integrity [31]. The development of wireless systems that can couple the mechanical properties with the sensor response without and any contact to the target specimen is one of the objectives in the development of magnetostrictive sensors. Several studies have been made following the Villari effect to archive this. This is done by increasing distance of the excitation coil from the specimen and still be able to generate longitudinal guide waves that could be picked up by another coil at a distance from the specimen. Jiang Xu [32] worked on this principles and lift-off effect on generating longitudinal guided waves in pipes. Using linear magnetostrictive stress in the presence of alternating magnetization, their fork followed this formulation of the lift off effect [32].

$$\sigma_{zz}^{ms} = -\frac{1}{2}\left(3\hat{\lambda} + 2\hat{\lambda}\right)(1-2v)m_z\frac{\partial\lambda}{\partial M_0} = -\frac{1}{2}\left(3\hat{\lambda} + 2\hat{\mu}\right)(1-2v)h_z\frac{\partial\lambda}{\partial H_0} \qquad (2.2)$$

Where $\hat{\lambda}$ and $\hat{\mu}$ are Lame constants, v is the Poisson's ratio, λ is the linear magnetostriction coefficient, M_0 is the magnetization of the static field in the z direction which is the axial direction of the pipe, m_z is the alternating magnetization in the z direction [32]. This work showed the decrease in efficiency of alternating current to strain with the increase in the distance between the coil and the specimen. Sensitivity of the sensor is affected by the increase in distance and this can be countered by the increase in current from the excitation coil [32]. Similar methods [21] [33] have been developed following the principles of Villari effect for SHM applications.

2.13 Wiedemann effect Sensors

Sensors that use this principle for SHM depend on the torsion produced in a current carrying ferromagnetic rod when subjected to a longitudinal magnetic field. This is a Wiedemann effect and was discovered in 1858 by Gustav Wiedemann [34]. The application of the Wiedemann effect sensors is not only in rods, but also hollow cylindrical shells. Two coils are used for the detection of this effect but with a different function from those used for Villari effect. Here, one coil generates a permanent magnetic bias while the other perpendicular to it provides time varying magnetic field and together creating in plane magnetic field. SHM sensors developed follow both Wiedemann effect and reverse Wiedemann effect difference being the orientation of the coils based on the desired wave propagation. Sergey Vinogradov and Adam Cobb [35] proposed a reversed Wiedemann effect sensors using the magnetostrictive material strip for testing of pipes and the other electromagnetic acoustic transducers used for testing tubes. The magnetostrictive transducer for testing of pipes demonstrated reduced impedance due to efficient solenoidal coil designs which also reduced power requirements increasing signal strength [35]. Sergey and Adam [35] also demonstrated that reversed Wiedemann uses switched positions of the permanent and

time varying magnetic field coils which resulted in strong biasing field strength with rare earth magnets.

Wiedemann effect sensors have also been developed for structures going through different loads that may result in structural damage or failure. Following the same principles of Wiedemann effect, Xiao-Wei [36] worked on the excitation of axisymmetric and non-axisymmetric guided waves in elastic hollow cylinders by magnetostrictive transducers. The circumferential structural health is monitored by relating the ferromagnetic magnetic guided waves propagation through the hollow pipe with mechanical states [36]. This work follows similar principles to that of piezoelectricity.

$$S = sT + dH \tag{2.3}$$

$$B = d^{T}T + \mu H \tag{2.4}$$

where **S** and **T** are strain and stress, **H** and **B** are magnetic field and magnetic induction, respectively, **s** is the elastic compliance matrix, **μ** is the magnetic permeability matrix, and **d**=∂**S**/∂**H** is the piezomagnetic coupling matrix. Xiao -Wei [36] also developed the stress monitoring sensor with a large static bias magnetic field $\bar{H}$ superimposed by a small dynamic magnetic field $\tilde{H}$ which can be related to the dynamic and static components of strain [36].

$$H = \bar{H} + \tilde{H} \tag{2.5}$$

$$S = \bar{S} + \tilde{S} \tag{2.6}$$

The directions of the small dynamic magnetic field and the static bias magnetic field were along the z and along theta respectively. This are related to the mechanical properties under the assumption of large static bias magnetic field, by the coupling matrix for torsional wave transducers [36].

$$d = \begin{bmatrix} 0 & 0 & 0 & 0 & 0 & \frac{3S_t}{H_{0\theta}} \\ -\frac{1}{2}\gamma & \gamma & -\frac{1}{2}\gamma & 0 & 0 & 0 \\ 0 & 0 & 0 & 0 & 0 & 0 \end{bmatrix} \quad (2.7)$$

For magnetostrictive materials used in this type of sensor, a high magnetostriction is necessary for a high Wiedemann effect. The study of the relation between the Wiedemann effect and the magnetostriction should be done. Li Ji-Heng and Gao Xue-Xu [37] worked on the Wiedemann effect of galfenol alloy. The magnetostrictive alloy was prepared by hot rotation. Longitudinal and circular fields are generated current in the solenoid and specimen from a DC power source [37]. Torsional stresses were applied to the samples at a specific twist angle and the magnetostriction measure using a standard strain gauge. Wiedemann twist showed an increase with the increasing magnetostriction [37]. This work also demonstrates that Wiedemann effect is also affected by permeability, elastic modulus, thermal expansion coefficient and other parameters. This proved the complexity of defining a clear relationship between the Wiedemann effect and magnetostriction effect [37].

2.14 Magnetovolume effect Sensors

In normal cases, the volume of the magnetostrictive material does not change. There are certain extreme cases where the volume of the magnetostrictive material may vary in the presence of magnetic field. This case happens in operations close to the magnetostrictive material curie temperature. This change in volume due to these effects is known as the Magnetovolume effect or Barret effect. The inverse of this principle is Nagaoka-Honda effect which is the change in the magnetic state due to a change in the volume [38].

2.15 Matteucci effect Sensors

This type of sensors working on the principle of Matteucci effect use amorphous magnetostrictive wires wound helically with exceptional magnetic properties. The principle is the thermodynamic inverse of the Wiedemann effect. Different methodologies of developing sensors using the Matteucci effect have been proposed. Using the detection of modulated Matteucci voltage due to torsional stresses on the ferromagnetic amorphous wire, Lassow and Meydan [39] developed an angular acceleration transducer. The natural frequency which was related to the Matteucci effect sensor response was derived following the principles torsion in circular rod [40].

$$T = \frac{G\theta J}{L} \tag{2.8}$$

Where T is the applied torsion or couple, J is the polar second moment of area of the wire, G the modulus of rigidity of the wire and θ is the angular twist over length. The sensor device developed by Lassow and Meydan [39] generated angular acceleration on the wire using the pin chuck while monitoring the Matteucci voltage change. The device was tested at different frequencies and magnetic fields to monitor the Matteucci voltage response which was proportional to the circular component of magnetization [39]. The stress sensitivity Matteucci voltage directly across ends of the wire did not need the use of pickup coils. This accelerometer demonstrated robustness and easy to construct. The device does not require supplementary equipment for signal conditioning and impedance conversion [39].

2.16 Change in E Effect Sensors

Young's modulus or modulus of elasticity (E) is the material property which denotes the stiffness of a material within its elastic limit. Magnetostrictive materials experience changes in elastic modulus in the presence of magnetic field. The effect of change in E due to varying magnetization

can therefore be applied in the development of sensors. The change in Young's modulus also depends on the mechanical stresses applied on the material. This relation of the magnetoelastic properties of a magnetostrictive material to the elastic modulus can be demonstrated using the linearized form of Hook's law [41].

$$\Delta\varepsilon = \left(\frac{1}{E^{H}}\right)\Delta\sigma + d\Delta H \tag{2.9}$$

$$\Delta B = d\Delta\sigma + \mu^{\sigma}\Delta H \tag{2.10}$$

Where $\Delta\varepsilon$ represents the changes in strain, ΔB is the changes in magnetic field, $\Delta\sigma$ is the stress variation and ΔH the applied field. Deferent developments have been made in SHM to develop sensors based on this phenomenon. Marcelo J. Dapino [41] worked on a model for the change in Young's modulus effect in magnetostrictive transducers. The work focused on the changes in the field induced hardening or ΔE effect at the applied DC magnetic field using Terfenol-D magnetostrictive material. It was illustrated that the changes in elastic modulus are positive in all bias field parameters even though thorough experimentation showed a negative ΔE at low bias fields due to magnetization jumps as shown in Figure 9 [41].

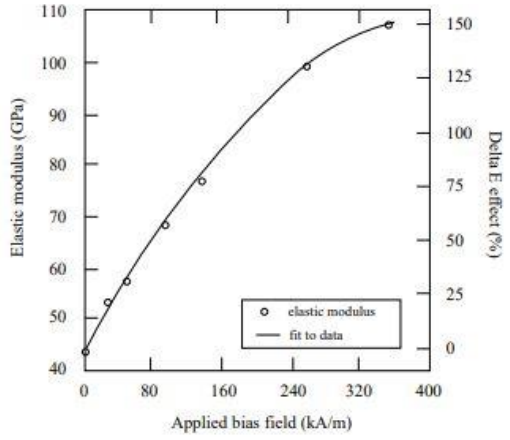

Figure 9. Young's modulus and changes versus bias magnetic field for Terfenol-D [15].

The continuous development of sensors that use the principle of change in Young's modulus in the presence of a magnetic field, strain and stress has led to different configurations of resonators. A tunable mechanical resonator using delta E in Terfenol-D magnetostrictive material is developed in this work [42]. A water-cooled transducer was designed for testing a Terfenol-D rod under quasi-static conditions, thermal, magnetic and mechanical operating phases [42]. The rod was placed in the center of the transducer and surrounded by pickup coil for magnetic induction. A cooling tube encased solenoid producing applied magnetic fields known as the Hall effect chip was placed at the midpoint of the rod [42]. The strain gauges placed on the rod resulted in the strains that were used to acquire the stress-strain curves as the rods are displaced and provide a measure of Young's modulus (E) [42]. When the realignment of magnetic moments easily occurs, the modulus was lower. It was realized that an increased magnetic field would allow a greater amount of magnetic moment reorientation resulting in lower modulus [42].

The current work done was on the development and investigation of a set of wireless magnetostrictive sensors embedded within the FRP composites for in-situ and real-time monitoring of local strains inside the composites. The voltage response during different test cases illustrated the working of the SHM technique developed in this work. The variation in sensitivity of the sensor at different loads is detailed and related with the development of cracks within the composite. This work therefore proves the working of the magnetostrictive sensor for SHM applications. This section details the procedure followed in the preparation of the sensor and the steps followed in the fabrications of composites embedded with micro-sized sensor. The testing methodology for the composite samples embedded with the micro-sized sensor is explained and details on a method used to relate the local deformations with the sensor detected strains shown.

2.2 Sensor Preparation

Sensors developed in this work were of two types of metglas materials. The 2826MB film and 2605SA1 film of an iron-nickel based alloy and an iron-boron-silicon alloy composition respectively. The process was done in a clean nano-fabrication lab. The sensor was first prepared for dicing into the required dimensions. Materials and equipment's used for this included silicon wafers, NR9-3000PY photoresist, oven hotplate and electro spinner. The silicon wafers were then cleaned with DI water and blow dried with nitrogen to remove inorganic residues. The wafer was then placed on the spinner and vacuum turned on to hold the wafer. The spinner speed was set to 2000 rpm in 40 seconds. Drops of the photoresist were then evenly distributed on the silicon wafer before spinning. The wafer was then spun for 40 seconds at 200 rpm as set. After this the photoresist of 1.8 µm was spread on the wafer and next the metglas sheet was then placed and pressed on the wafer. To solidify the photoresist, the wafer with metglas films attached was then baked on a hotplate at 120^{o} C for 60 seconds.

The metglas films were then taken to the Dicing Machine (Disco DAD3220 Automatic Dicing Saw, 160mm). Before dicing, a few steps were followed to make sure that the machine is provided with accurate information about the dicing blade. First the height of the blade was verified. The machine first lowered the blade to contact the edge of the chuck. This verified that the machine was able to read when it is encountering resistance. The next part of the sequence was to move the blade to the back sensor and move up and down through the sensor. This detected where exactly the outer edge of the blade was and would alarm if there was significant enough deviation from the expected value. The wafer was then divided into single units, or dice. Units of sizes 16 mm × 4 mm were diced. A rotating abrasive blade performed the dicing, while a spindle at high speed, 30,000 to 60,000 rpm, rotated the blade. During the separation of dice, the blade crushed the wafer

and removed the created debris simultaneously. Material removal occurred along dedicated dicing lines between the active areas of the dice. When the dicing blade moved along these streets, a groove was formed in the substrate material. The groove width was proportional to the thickness of the blade. Upon completion, the wafer was the retracted and the diced sensor removed.

2.3 Device Fabrication

This section gives detailed steps on the fabrication of the sensor response detection device used in this work. The device was fabricated in a nanofabrication clean room to control the number of contaminants. This is because critical components for the device were at a very small scale and require precise dimensions. The first step in this section was to design a mask pattern to be used in the photolithography process. The pattern was based on the planar coil dimensions required for the magnetostrictive sensor. 5-inch wafers were used in this work and steps followed in their cleaning process is detailed. Photolithography steps followed in this work is therefore detailed and how the fabricated components were connected is given.

2.31 Materials

In the initial step of the pattern design, AutoCAD was used. A chrome 5-inch mask was used as it matched the aligner in the photolithography process. Wafer cleaning process followed in this work was the RCA and HF wafer precleaning. P-type 4-inch diameter wafers were selected to be used for the fabrication of the planar coil devices. In the process of pre-cleaning the silicon wafer, chemicals were used. Correct procedures, protocols and safety measures were taken. Sulfuric acid, hydrogen peroxide, deionized (DI) water, ammonium hydroxide, hydrochloric acid (HCL), oxygen, nitrogen and silicon wafer were used in this work.

2.32 Mask design

Photomasks are designed to optically transfer a pattern to a target substrate in most cases a wafer. They are chrome coated and based on the design masks can be clear field or dark field. In this work, the planar coil design was done in the AutoCAD package. Four-layer pattern was designed with critical dimensions of 20 µm. The first layer was of the actual planar coil include the center and outside connecting pad, second layer was to open up the connecting pads after insulation, forth layer was transfer the center connecting pad to the outside section of the planar coil and final design was to open up the connecting pads after insulation. Alignment markers were placed on each layer to maintain the positions of all the patterns on each layer. Figure shows all the four-layer masks.

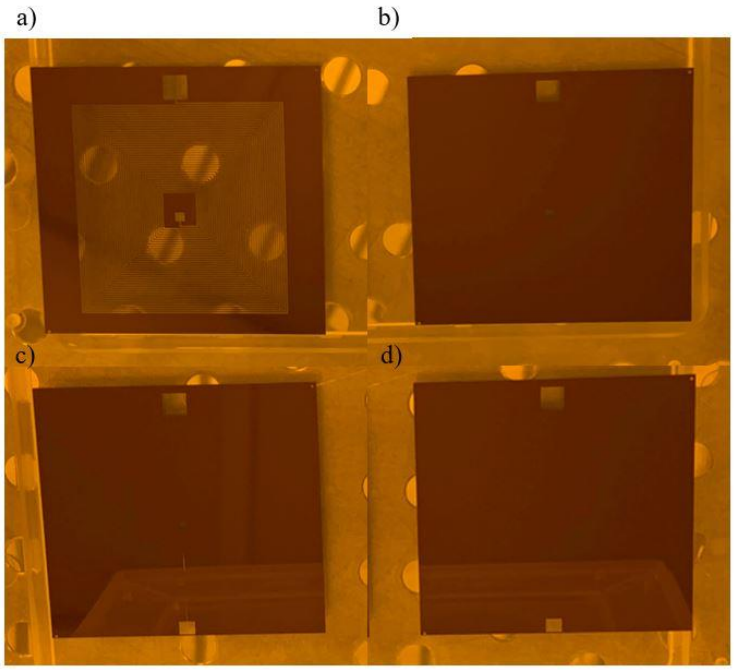

Figure 10. a) Shows the first pattern of the planar design, b) second pattern for opening connections, c) transfers the center connection towards the edge and d) opens the connections after insulation.

These designs were then formatted and transferred to a 5-inch mask glass coated with chrome. A dark field mask was made for all the patterns as the intention for these devices was to use a positive photoresist. The completed mask was taken to the cleanroom and the process of pre-cleaning the wafers to be patterned started.

2.33 Wafer Cleaning

In this step of the experimentation, the chemical and solvent hoods were used. The user wore rubber gloves for protection from acids and chemicals, protective sleeves for extra protection from chemicals and non-reactive apron for frontal protection. Making the solution of piranha was the initial step. The purpose piranha cleaning was the removal of any residues from the wafer. The solution was made from a 3:1 ratio of a mixture of concentrated sulfuric acid (H_2SO_4) with hydrogen peroxide (H_2O_2) respectively. The acid is then added to water and should never be done the other way around and then warmed on a hotplate to 90-110^{o}C[18]. A thermometer is used to measure and adjust the solution temperature. This solutions or mixtures require extra safety measures as they are highly reactive to heat while separate, even though the response in the acid piranha can start by itself unlike the base one which requires the presence of heat to 60 degrees beforehand the reaction.

There are many things which could cause the reaction to accelerate out of control. If one provides sufficient fuel for them such as photoresist or IPA they will generate enormous quantities of heat and gas. For these reasons, chemical safety procedures are strictly followed. This was an exothermic chemical reaction. The wafer placed on a wafer holder were then placed in the solution for 10 minutes. A clean quartz wafer holder was used. The wafers are then removed and rinsed in DI water vigorously followed by blow drying with nitrogen. The nitrogen pressure was controlled to avoid wafer cracking or breakage.

Another solution of 1:1:10 ratio entailing ammonium hydroxide (NH_4OH), hydrogen peroxide (H_2O_2) and deionized (DI) water (H_2O) respectively was made. The solution was then placed on a hotplate and warmed to temperatures of 70^{o}C. A thermometer was used to monitor the temperature change during this step of the experimentation. Upon completion of making the solution, the silicon wafers were then immersed in it for 5-10 minutes. After this time the wafers were then rinsed again in DI water followed by dry nitrogen drying to remove residual organic films, metal resides and dust particles. Last step in chemical pre-cleaning of the wafer was the preparation of hydrochloric acid (HCL), hydrogen peroxide (H_2O_2) and deionized (DI) water (H_2O) of ratio 1:1:10 respectively. This solution was warmed to a temperature of 80^{o}C. After formation of this solution, the substrates are then deep in the solution for 5-10 minutes. The wafers are the washed in DI water and blow dried with nitrogen. When the water evenly flows over the surface of the wafer depicts how clean they are. It should be noted that bare silicon is hydrophobic while silicon hydroxide is hydrophilic. This last step removed the atomic and ionic contaminants on the wafer surface. This therefore completed the process of pre-cleaning the wafer.

2.34 Photolithography

This is part gives steps of how the wafer was patterned. First the beakers were prepared with developer and DI water for rinsing the wafers. The wafers were already coated following the steps in the previous section and soft baked at 120^{o}C for 120 seconds. From the specification sheet the optimum exposure energy of SR1813 positive photo resist is 140mj/cm2. The pattern was taken to the aligner and exposed for the first wafer at the energy of 6.1 mW/cm2 × 3 sec which is equal to 18.3 mJ/cm2. The power level of 6.1 mW/cm^2 in constant intensity (CI) mode, 8.4 mW/cm^2 in constant power (CP) mode for the MJB3 mask aligner, was the normal value of the equipment setting. These was repeated for all wafers.

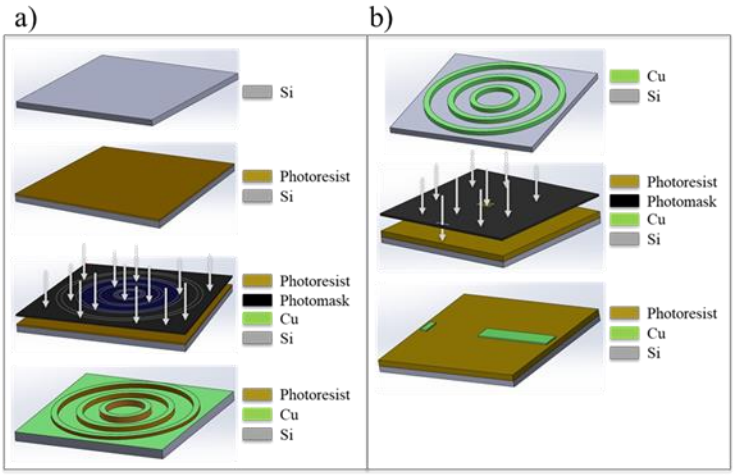

Figure 11. Section a) Shows a clean silicon wafer, a spun coat of photoresist 7.5 µm thickness, mask and UV exposure under an aligner, and sputtered titanium and cupper layers. b) Shows the copper layer after lift-off, UV exposure to transfer inner connection pad to the edge and the final device after lift-off.

The next step was the post exposure bake. In this step, the wafers are baked at 120^{o}C for 120 seconds after exposure. Using the tweezers or Teflon holder for 4" wafers, the wafers were then immersed in the developer (MF319) for 22 seconds. The wafers were held and agitated by moving the wafers back and forth once per second roughly. After these steps the pattern was now visible 10 to 20 seconds before the completion of the development stage. The wafers were then removed and quickly transferred to the DI wafer and rinsed for 30 seconds with similar agitation. The wafers were then placed on a cloth and blow dried gently with nitrogen. After this the wafers were inspected under a microscope and the integrity of the pattern was recorded. The main priority was to determine the clearance of exposed area from resist. The pattern that is badly deformed meant that the wafers were not developed long enough, or the exposure was not enough.

A layer of copper was sputtered on the wafer and etched out to leave the designed planar coil. With the addition of other steps, the planar coils fabrication was completed. These two coils were

connected to two SMA connectors. The objective was to use one coil as a pickup and the other as an excitation coil. This therefore completed the fabrication of the sensing device.

2.4 Composites Fabrication

VARTM process was followed for the fabrication of all composite samples in this work. The fabricated composites contained four plies of fiber in unidirectional 0^o orientation. This process involved integrated mechanisms. The mold used for fabricating the composite panel was an aluminum metal plate laminated with vinyl mold release compound. The vinyl mold release compound is applied on the aluminum mold to aid the detachment of the composite from the mold upon completion. The setup involved two layers of peel ply with dimensions 1 inch more than that of the fiber mats size. The first peel ply was placed on the vinyl mold release compound. Then followed layers of selected fibers. Four plies for both CFRP and GFRP of sizes 10x7 inches were laid-up. The developed sensors were between two fiber plies. The last step in laying up the VARTM setup was cutting a vacuum bag of suitable size that covered the entire mold plate. The setup was sealed, and next resin tubing inlets and vacuum inlets connected. The vacuum inlet was connected to a vacuum pressure that was used to maintain a vacuum pressure above 25bar throughout the process. This resin tubing was connected to an epoxy containing with epoxy resin being drawn in the vacuumed layup. Epoxy resin made from diglycidyl ether of Bisphenol-F and a polyamine curing mixture was used as a polymer matrix. Due to low viscosity of the resin at the time of infusion in the layup, the process was completed in a short time for each batch of samples. After the spread of the resin throughout the fibers, the pump was disconnected from the pressure valve, which still maintain vacuum pressure within the setup. It took 24 hrs. for the resin to cure. Upon curing, the composites embedded with sensors were cut into strips of 1.5 cm × 1 cm as shown in Figure 12 schematically.

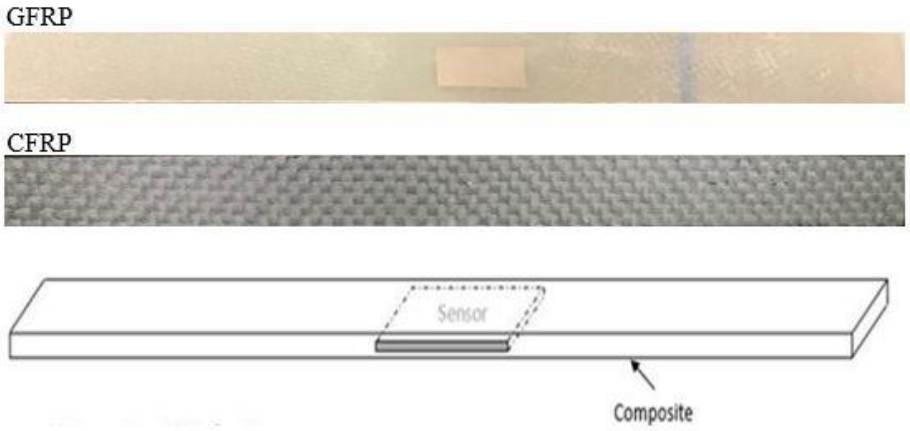

Figure 12. Fabricated composite samples embedded with sensors.

2.5 Testing Methodology

In this section, the testing methods followed for composites embedded with sensors are detailed. Multiple samples were tested following different mechanical testing methods. The aim of each mechanical testing procedure in this work was to monitor the sensors response with the development of deformations within the composites during different loads. The tests were conducted for composites with metglas sensor and terfenol-D particles sensors. Continuous tensile test, discrete tensile test and dynamic loading for fatigue test were conducted. The testing setup for all this measurement was on the MTS hydraulic testing machine. These tests were characterized based on sensor embedded composites investigated; composites with metglas 2826MB sensors, composites with metglas 2605SA1 sensors and composites with embedded Terfenol-D sensors as further explain in the next subsections.

2.51 Continuous Tensile Loading

The three types of composites fabricated in this work were passed through continuous and discrete tensile loading. Each type was tested under uniaxial tensile loading using an MTS Servo-hydraulic test system. The designed planar coils were used, one as an excitation coil placed at 0.5cm from

the surface of a composite sample during testing and connected to an alternating current voltage source and the other still 0.5 cm from the composite to pick up the magnetic flux change during the tensile loadings, as shown in Figure 13. Discrete measurements and continuous measurements were both taken during uniaxial tensile loadings. For the discrete measurement, a tensile load was applied at three different load levels: 2 kN, 3 kN and 4 kN. At each of these three load levels, sensor measurements were picked up by the planar coil over frequencies ranging from 0 Hz to 5 kHz. The continuous measurements were taken at 50 kHz and 100 kHz up to 6 kN, which was above the breaking load of most composite samples.

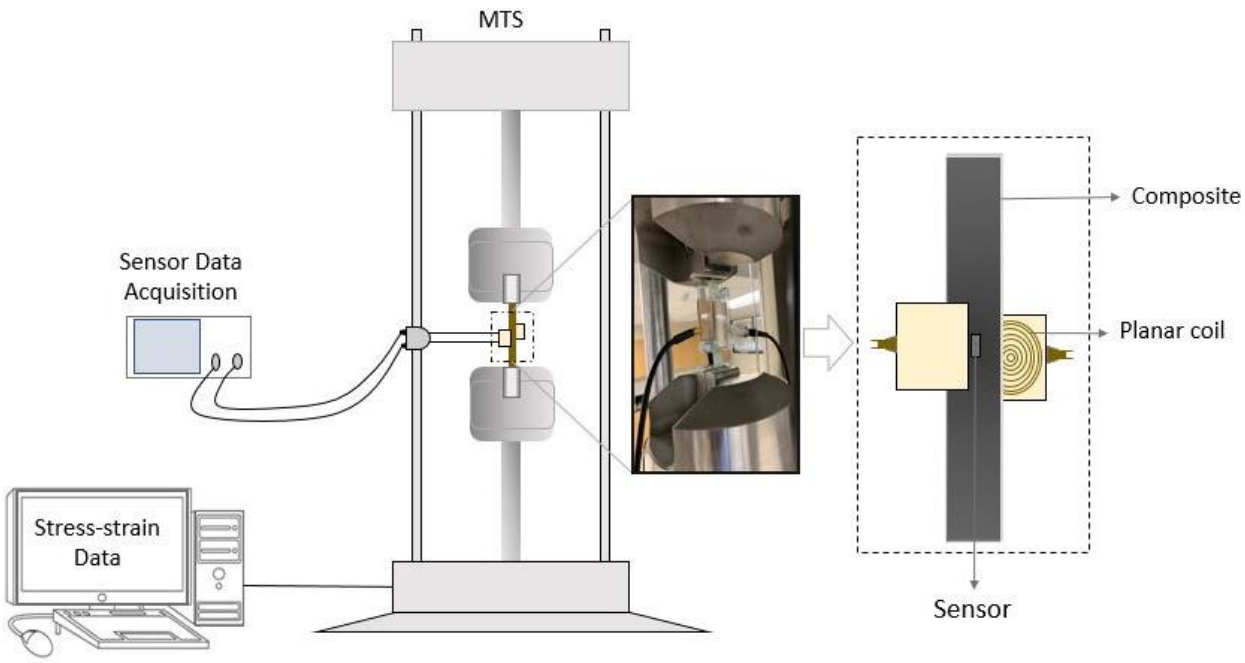

Figure 13. Composites continuous tensile loading.

2.52 Imaging Methodology

The composite samples in this work were examined with the hirox microscope to achieve the image resolution required. The replica technique used involved softening an acetate tape in

acetone, applying it to the composite surface, and then allowing it to harden as acetone evaporates. After careful removal from the surface, the acetate tape contains a negative image, or replica, of the composite surface that can be directly examined. These steps were done during tensile loading of the sample from 0 loading to 1 kN, a 60 seconds break was taken for imaging. Tensile loading was then continued for another 1 kN to 2kN. After this, loading was paused for 60 seconds and the replication process repeated. This was done for multiple intervals until the composite failed. Double-faced tape was used to bond the replica to the glass slide to obtain large, flat, undistorted replica surfaces. The advantages of this process include getting a permanent record of the specimen is obtained, better resolution and higher magnification can be used, and contamination of the polished surface is minimized.

2.6 Results and Discussions

This section gives details of all the experimentation done in this work to characterize the properties of this sensor. The change in properties of the composite structure is also relayed in this section. First the sensor surface tested properties are explain followed by all mechanical tests done on the composites embedded with the sensor material.

2.61 Sensor Surface Properties Tests

The selected metglas sheets surface properties were analyzed and improved to better adhere to the composite. This study was done on metglas 2826MB sheet and metglas 2605SA1 sheet composed of iron-nickel and iron-boron-silicon respectively. The magnetostriction of the 2826MB sensors is 12 ppm and for 2605SA1 is 27 ppm. The surface properties of the sensor materials were considered by investigating the surface energy of the materials. The surface energy was determined using Kruss Mobile Surface Analyzer (MSA) [43]. The MSA used two liquids to determine the surface energy, water as the polar one and diiodomethane as the nonpolar one. Two drops from these liquids were

then placed on the surface and the contact angles were determined. The results of the surface energies for the sensor materials are shown in Table II.

Table II. Surface energy for the magnetostrictive sensors.

Sensor Types	**Disperse (mN/m)**	**Polar (mN/m)**	**Surface Free Energy (mN/m)**
Smooth Sensor Surfaces			
2826MB	31.96 ± 0.98	0.34 ± 0.01	32.30 ± 0.97
2605SA1	33.76 ± 0.63	0.22 ± 0.03	33.98 ± 0.60
Rough Sensor Surfaces			
2826MB	46.69 ± 1.25	0.12 ± 0.03	46.81 ± 0.95
2605SA1	47.43 ± 0.23	0.31 ± 0.02	47.74 ± 0.21

The surface energies of the smooth sensor surfaces were 32.30 mN/m and 33.98 mN/m, and of the rough sensor surfaces were 46.81 mN/m and 47.74 mN/m, for the 2826MB and 2605SA1sensors, respectively. This indicated a better adhesion between the rough sensor surfaces and the FRC in comparison with the smooth sensor surfaces. Dimensions of the sensors made from these two types of materials are 1.5 cm by 1 cm by 15 μm. These dimensions were selected to provide sufficient sensor surface areas whereas small thicknesses comparable to the thickness of each composite layer.

2.62 Continuous Tensile Tests

The response of the GFRP composite embedded with 2826MB sensor during continuous tensile loading is shown in Figure 14. The sensor output voltage increases linearly at low strains. With further increase in strain, the sensor output voltage shows a considerable non-linear response. This irregularities in sensor output were attributes of different elastic properties between the sensor and GFRP. It is shown that the specimen exhibits an average peak stress value of 250MPa and an average strain value of 2.30 % ε which is around 2600N load value. Using 100 kHz detection frequency, the sensor output voltage increases nearly linearly with the increase in strain upto 1.7 % ε, and continued to increase with a steeper slope until it reaches a maximum at 2.3% ε. The sensor output past this point gives a steady response as the overall composite strain continues to increase. The sensitivity shown by the 2826MB sensor for the measurement at 100 kHz is 4.12 μV/με and the sensitivity at the 50 kHz measurements is of 6.667 μV/με.

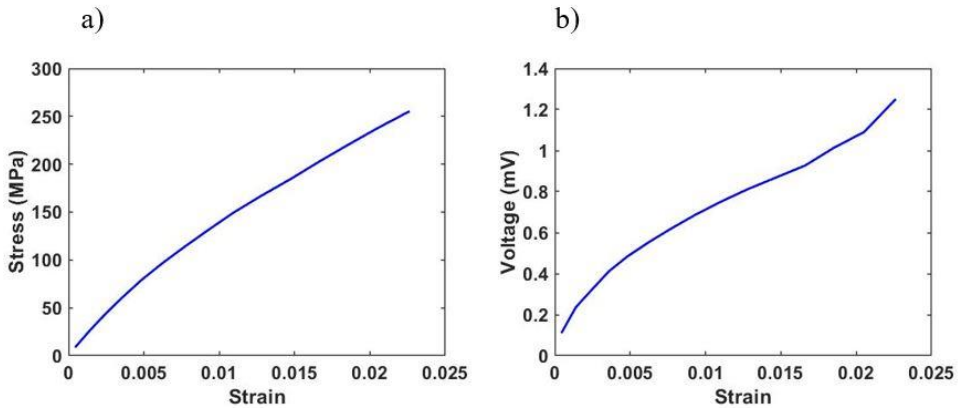

Figure 14. a) Shows the stress-strain response of the 2826MB sensor embedded GFRP composite and b) give the voltage response of the same type of composite.

The development of defects within the composite during tensile loading were imaged using replicating tape and Hirox microscope. Figure 15, shows no defects at initial loading. As loading increases with the voltage response, the development of cracks is noticed. The load, stress and

strain graphs showed a linear distribution, as time and force increase. It is seen that the composite experiences a brittle fracture showing linear deformation at low and high stresses. The high strain rate tensile testing data shows that the glass fibers can stiffen with increase in strain rate around the plies which is known as anti-buckling effect. Increase in loads applied on the composite sample to 2kN resulted in the development of minor cracks in the composite shown on image b). The development of defects within the composite show an increase in the metglas 2826 sensor response. Further loading of the GFRP composite resulted in the propagation of these minor defects into cracks shown in c) within the composite. The development of cracks results in decrease of dampening of the sensor response and therefore an increase in the detection of sensor Villari effect. An increase in slope of the voltage response is observed at 11 seconds and 0.85 mV. The size of cracks developed on the composites structured increases with increase in loading until the composite failed at 0.24 % ε.

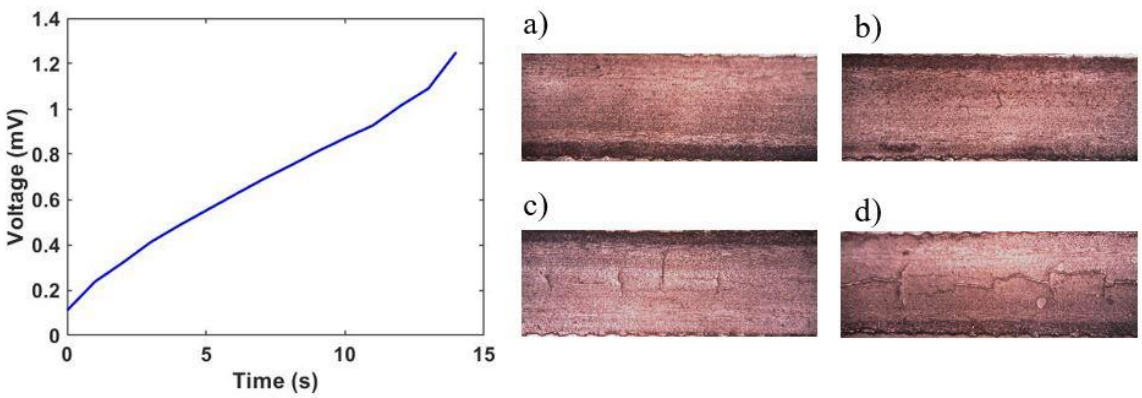

Figure 15. The metglas 2826MB sensor embedded GFRP composite voltage response in time is shown, coupled with a) structural health prior loading, b) at initial loading, c) at 3 kN loading and d) 4kN loading towards failure.

A similar experimentation was done for composite samples embedded with metglas 2605SA sensors. Figure 16 shows the response of the composite embedded with 2605SA1 sensor during continuous tensile loading. The sensor voltage response at low strains increases linearly with strain

and on further loading, the slope of the sensor voltage response decreases as the strain continues to increase. The sensitivity shown by the embedded sensor is 5.7 μV/με for the measurement at 100 kHz and 10.30 μV/με for the measurement at 50 kHz. Compared with our recently reported thick embedded sensors which were 30 μm in thickness [29] , the embedded sensors using thinner sensor materials shown in this work provide strain sensitivities at larger ranges of strains, covering both low strain and high strain regions.

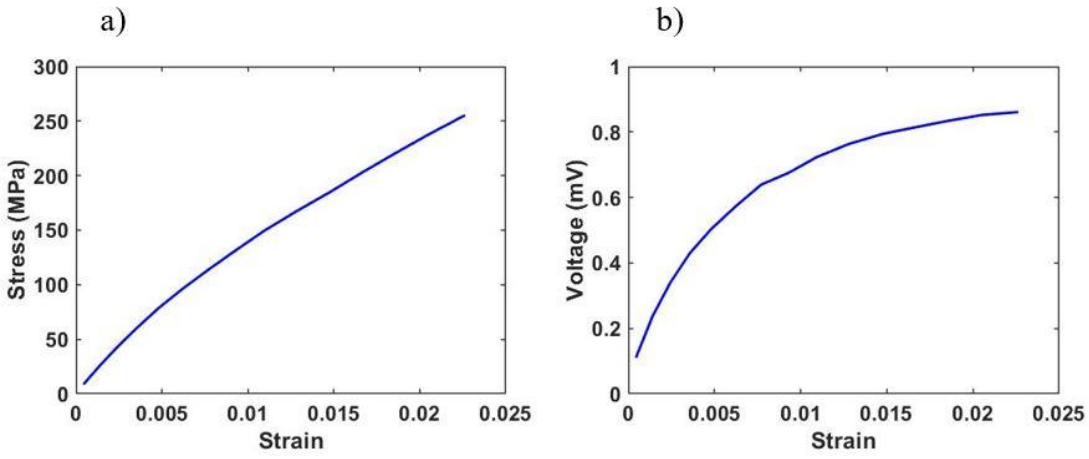

Figure 16. a) Shows the stress-strain response of the 2605SA1 sensor embedded GFRP composite and b) give the voltage response of the same type of composite.

GFRP composites embedded with metglas 2605SA1 sensors showed a trend like that of composite embedded with 2826MB sensor. The difference is observed from the sensor response at high strains. Metglas 2605SA1 Villari effect showed a voltage response of lesser sensitivity from 1.4 % ε to composite failure. The change in sensor voltage response from 5 to 15 seconds point is much less than that of metglas 2826MB embedded composites. The position of the sensor within the composite also influences the size and propagation of defects. Figure 17 shows the distribution of defects for this sample resulting in cracks of bigger sized compared to those of samples embedded with metglas 2826MB sensor.

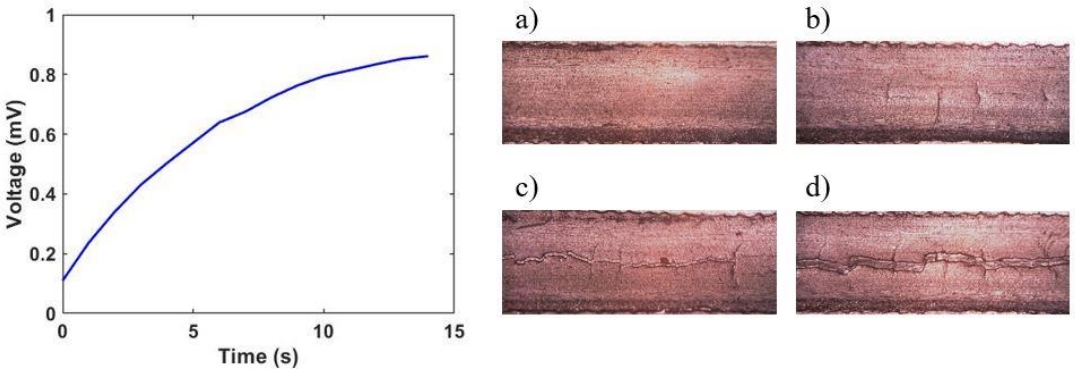

Figure 17. The metglas 2605SA1 sensor embedded GFRP composite voltage response in time is shown, coupled with a) structural health prior loading, b) at initial loading, c) at 3 kN loading and d) 4kN loading towards failure.

Finally, the same experimentation was done using the powdered sensor type with higher voltage response compared to the metglas sensors. Terfenol-D sensors were designed to match the same line of setup used for other tests. That means the sensor covered the same area within its composite sample as the other sensors. At very low strains, Terfenol-D showed a jump in voltage response for every test to a range of 0.6 mV which was an average response for metglas 2826MB and 2605SA sensors. With a lower sensitivity, the sensor response further increased to 4.5 % ε.

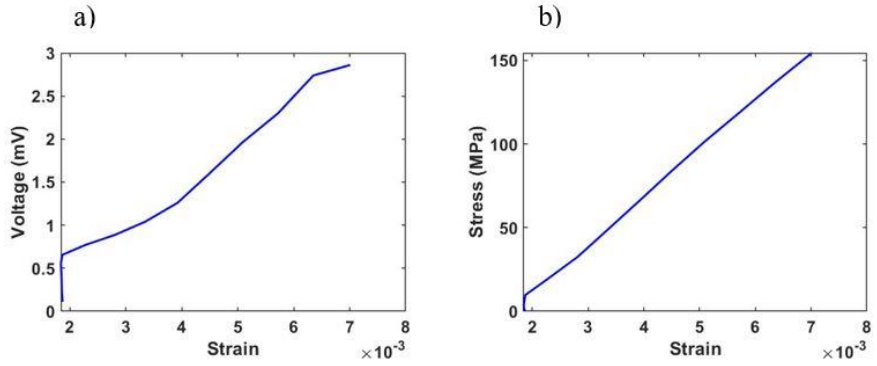

Figure 18. a) Shows the stress-strain response of the Terfenol-D sensor embedded GFRP composite and b) give the voltage response of the same type of composite.

Imaging of the GFRP composites embedded with terfenol-D at initial loading did not show any defects due to loads. From 4.5 % ε, the steepness of the voltage response increases at a higher rate

in turn defects leading to the development of matrix cracks were observed as shown in Figure 19 c). At high strains, terfenol-D embedded composite sensors showed a decrease in sensitivity as deeper cracks develop within the structure shown in Figure 19 d).

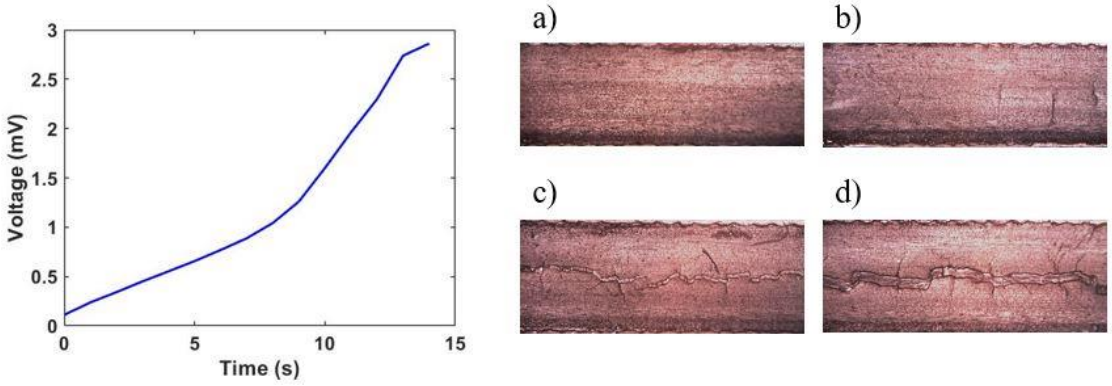

Figure 19. The metglas Terfenol-D sensor embedded GFRP composite voltage response in time is shown, coupled with a) structural health prior loading, b) at initial loading, c) at 3 kN loading and d) 4kN loading towards failure.

A comparison in properties of the developed sensors was done using a different composite samples. Carbon fiber reinforced polymer (CFRP) composites was selected for batch or tests like those done for GFRP composites. Differences were observed due to the difference in elastic properties of these two materials. Metglas 2826MB sensors embedded in CFRP composites showed a high sensitivity of 6.78 μV/με at lower strains. The sensor voltage response was linear for the initial loading from 0 to 1.3 % ε. Samples embedded with metglas 2826MB seemed to fail earlier than the rest of the samples at 1.8 % ε. A further increase in voltage response with a continuous decrease in slope was observed up to composite failure. A varied sensor response was observed in metglas 2605SA1 CFRP sensor embedded composites. The voltage response at lower strains up to 0.7 % ε showed higher sensitivity of 7.6 μV/με. Further loading of this samples resulted in a decrease in voltage response change from 0.6 mV to 1.1 mv giving a delta of 0.5 mV. This was a maximum voltage response for GFRP composites embedded with similar sensors.

From strains of 0.75 % ε, an increase in voltage response within linearity was observed till composite failure. A more stable response in CFRP composites embedded with Terfenol-D was observed. An increase in voltage response with sensitivity of 7.2 μV/με up to strains of 0.92 % ε was reflected. Further increase in loads showed an increase in Terfenol-d sensitivity to 10.2 μV/με. Linear sections throughout loading of Terfenol-D embedded sensors were observed and a slightly lower voltage response was observed for these powdered sensors. This may be because of their distribution within the composite plies as due to lack of visibility through CFRP composites, perfect sensor dimensions for Terfenol-D was not achieved.

2.7 References

[1] G. M. Light, H. Kwun, S. Kim, and R. L. Spinks. "Magnetostrictive sensor for active health monitoring in structures." 4702 (2002): 282-288.

[2] Joseph L Rose, Jason K, Van Velsor, Steven E. Owens and Roger L Royer. "Magnetostrictive sensor array for active or synthetic phased-array focusing of guided waves." US13/298 (2011).

[3] Sujjatul Islam, Relebohile G. Qhobosheane, Muthu R.P. Elenchenzhian, Vamsee Vadlamudi,Rassel Raihan, Kenneth Reifsnider, Wen Shen. "STRUCTURAL HEALTH MONITORING OF FIBER-REINFORCED COMPOSITE USING WIRELESSMAGNETOSTRICTIVE SENSORS." Proceedings of the SAMPE Conference 19 (2019).

[4] A. Al-Hajjeh, E. Lynch, C. T. Law, and R. El-Hajjar. "Characteristics of a Magnetostrictive Composite Stress Sensor." IEEE Magn. Lett. 7 (2016): 1-4.

[5] M. A. Haile, A. J. Hall, J. H. Yoo, M. D. Coatney, and O. J. Myers. "Detection of damage precursors with embedded magnetostrictive particles." Journal of Intelligent Material Systems and Structures 27.12 (2016): 1567–1576.

[6] Jiang Xu, Yong Sun, and Jinhai Zhou. "Research on the Lift-off Effect of Receiving Longitudinal Mode Guided Waves in Pipes Based on the Villari Effect." Sensors (Basel) 16.9 (2016).

[7] Z. H. Żurek, G. Dobmann, P. Idziak, K. Kowalski, and P. Poznańska. "SHM-STRUCTURAL HEALTH MONITORING AND NDT FOR THIN STEEL SHEETS UNDER LDC TESTING WITH A FLAT ASYMMETRIC PCB SENSOR." (2019).

[8] F. K. Lane, G. Otis Smith, J. H. Lewis We, and H. C. Holtz Washington. "DEPARTMENT OF THE INTERIOR UNITED STATES GEOLOGICAL SURVEY." (2019).

[9] S. Vinogradov, A. Cobb, and J. Fisher. "New magnetostrictive transducer designs for emerging application areas of NDE." Materials (Basel) 11.5 (May 2018).

[10] X. wei Zhang, Z. feng Tang, F. zai Lv, and X. hong Pan. "Excitation of axisymmetric and non-axisymmetric guided waves in elastic hollow cylinders by magnetostrictive transducers,." J. Zhejiang Univ. Sci 17.3 (Feb 2016): 215–229.

[11] J. H. Li, X. X. Gao, J. Zhu, X. Q. Bao, L. Cheng, and J. X. Xie,. "Wiedemann effect of Fe - Ga based magnetostrictive wires,." Chinese Phys. B, 21.8 (Aug. 2012).

[12] Grunwald, A. G. Olabi and A. "Design and Application of Magnetostrictive 'MS' Materials." 11165967 (2009).

[13] Meydan, R. Lassow and T. "An Angular Accelerometer using Amorphous Wire." IEEE Trans. Magn 31.6 (199): 3179–3181.

[14] William Thomson Baron Kelvin, Peter Guthrie Tait. Principles of Mechanics and Dynamics. 1962.

[15] M. J. Dapino, R. C. Smith, and A. B. Flatau,. "Model for the ΔE effect in magnetostrictive transducers." Smart Structures and Materials 3985 (2000): 174.

[16] Kellogg, R. A. "The Delta-E effect in Terfenol-D and its application in a tunable mechanical resonator." (2000).

[17] Johnson, Kenneth Langstreth, Kevin Kendall, and A. D. Roberts. "Surface energy and the contact of elastic solids." Proceedings of the royal society of London. A. mathematical and physical sciences (2001): 301-313.

Chapter 3: Smart Self-Sensing Composite Fabrication and Development

3.1 Introduction

The development of smart self-sensing composite materials has been prominent in recent years. This is due to the need for advanced nondestructive structural health monitoring methods[1]. Composite materials during fabrication and operation go through a series of stresses. This includes shear stress, normal stress, torsional stress, bending stress or combined stresses. The resultant deformations from these stresses bring about various types of composite defects. The defects can be microscopic defects which are sometimes negligible but can affect the strength of the overall composites or they can be macroscopic which are due to the composite structural features[2]. The types of defects generated within a composite material depend on the cause of deformation. During the manufacturing process of composite materials, small holes may be generated within the system increasing its porosity. This results in the formation of voids defects within a composite which may lead to the generation of cracks. Voids can also be generated within the composite during its operation due to different environmental changes such as temperature, pressure and other types of loadings. Delamination is another defect type that may results due to different loading conditions on the composite sample. Propagation of minor defects such as voids and matrix cracks can also leady to delamination within a composite sample[3].

Composite materials mechanical properties highly depend on the types of constituents incorporated in its fabrication. This also contributes to the types of defects generated within the composite system. There are numerous methods developed to detect defects and their precursors within the composite structure[4]. Common damage detection methods include systems that

connect detecting probes on the target specimen. This mechanisms that introduce foreign materials within a composite degrade the structural integrity of the composite. Therefore, this brings forth the need for non-destructive structural health monitoring systems. There are different types of NDT methods which include ultrasonic surface waves detection, ground penetration radar, electrical resistivity sensors, half-cell potential and impact echo detection systems[5]. This work focuses on the development of a piezoelectric magnetostrictive self-sensing smart composite and the construction of an advanced magnetostrictive sensing capability.

The use of piezoelectric materials in smart composites development has shown great strides in recent years. In the manufacturing of composites, carbon nanotubes have attracted the most attention. Numerous studies have focused on this, including Denish Kumar[6] worked on the on the characterization of glass fiber composites with multi walled carbon nanotubes at high temperatures. Comparisons of MWCNT volume fractions to fiber volume fraction was done and mechanical tests conducted to study the stress strain response at higher temperatures[6]. This work showed that 0.1% MWCNT in glass fiber composites contributes to the increase in flexural strength and modulus of the composite[6]. This worked also showed that higher temperatures had higher impact on glass fiber composites incorporated with MWCNTs than conventional glass fiber composites[6]. Studies like [7] focus on the manufacturing process of CNT glass fiber composites. CNT-epoxy nanocomposites were coated on the glass fiber. This work explored the effects of shape, size and surface chemistry of CNTs that contributed to their agglomeration [7]. It was proven that composite samples coated with CNTs have improved tensile properties [7].

Sputtering of a specific combination of this rare earth magnetostrictive materials in amorphous alloys can yield a material with a high magnetostriction. The same principle followed in creating magnetostrictive materials can be used to introduce additional materials such as metals, glass,

concrete, ceramic, composites, polymers or other materials to develop smart magnetostrictive composites for specific applications. For energy harvesting applications, magnetostrictive alloys such as FeCo alloys can be combined with alloys such AlSi with good stress strain transfer to create a favorable composite[8]. This is done by melting FeCo and forging it into required fibers. These fibers are then embedded into melted AlSi to form a FeCo/AlSi composite that can be used for voltage generation with the application of stresses[8]. Magnetostrictive smart composite such as this require extensive comparison study to achieve perfect fiber to matrix weight fractions.

FeCo alloy can also be used in the development of smart composites for sensing applications. The drawn FeCo fibers mixed with diglycidyl ether of Bisphenol-F and a polyamine curing agent for matrix results in a FeCo fiber reinforced composite sensitive to bias magnetic field changes[9]. The alignment of the magnetization vector with the bias magnetic field in this type of smart magnetostrictive fiber reinforced composites contributes to its sensing properties[9]. Due to its magnetostrictive property, any change in magnetic field generates a mechanical response from the sensor. Further developments of magnetostrictive composite materials are explored in the development of whisker sensors[10]. Alfenol and galfenol alloys are melted with other metals, cold rolled to the required thickness and annealed to thin sheet samples[10]. The magnetostrictive materials are wrapped with plain weave carbon fiber and epoxy. The fabricated smart composite can therefore induce magnetization as result of applied stress[10]. Numerous studies [11][12]have contributed to this area in developing smart composites. In this work, Terfenol-D magnetostrictive materials is used to develop a smart self-sensing fiber reinforced composite.

3.2 Experimental Methodology

The development of the piezoelectric magnetostrictive self-sensing composites in this work was completed in two steps. First was the design and fabrication of the composite, detailing the

constituents in this composite to give it its piezoelectric and magnetostrictive properties. The next step was the development of the detection method used. To experimentally characterize the smart self-sensing composite piezoelectric and magnetostrictive response, an advanced magnetic flux density and electrical change detection device was developed. The composite specimens were run through a series of mechanical tests to explore their self-sensing capabilities and limitations for further research and applications.

3.21. Piezoelectric Solution

The fabrication of smart self-sensing composites in this work followed a unique approach. Terfenol-d nanoparticles were used for sensing material and carbon nanotubes for the improvement of the composite mechanical properties. The preparation of SWCNTs in this work also followed a unique approach. Single-walled nanotube from Sigma Aldridge with an inner diameter of 0.7–1.1 nm were used. These SWCNT had chirality of 7.6, and the materials used for preparation were nitric acid (HNO_3), sulfuric acid (H_2SO_4) and isopropanol. The properties of SWCNTs due to their van der Waal forces lead to their agglomeration. For the purpose of this work, agglomeration of SWCNTs was evaded by functionalizing the SWCNTs in acid. Exohedral functionalization was followed by dispersing 50 mg of SWCNTs in 150mL of 1:3 $HN0_3$: H_2SO_4 solution under 120 °C heat and stirred at 500 rpm. After acid treatment of this SWCNTs, deionized (DI) water was used to clean the material thoroughly. The next step was ultrasonication in isopropanol of the SWCNTs for 1 h. Hydroxyl and carboxyl groups that can interact with oxygen containing groups in glass fiber prepreg were generated from chemical oxidation. The ultrasonicated solution was then dispersed on prepreg fibers for composite fabrication. These steps are summarized in Figure 1a. The electrical field was then applied to the prepreg with SWCNTs, as shown in Figure 20, to alter their orientation. SWCNTs rotate and shift to form a head-to-head

contact moving towards the negative electrode, therefore forming developing and aligned networks.

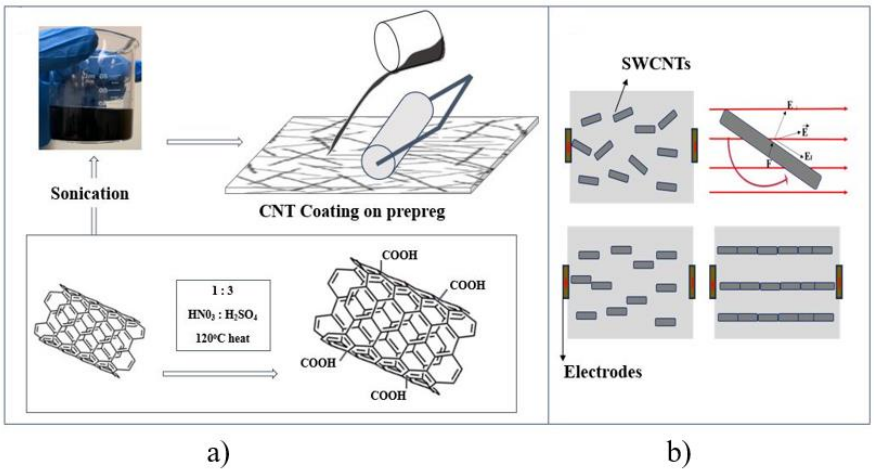

Figure 20. Steps followed in (a) the fabrication of SWCNT fiber composite and (b) alignment of SWCNTs.

3.22. Magnetostrictive Solution

To develop a self-sensing composite with magnetostrictive properties, Terfenol-D particles were added as part of the final composites. To do this, the epoxy diglycidyl ether of Bisphenol-F and a polyamine curing agent matrix were mixed with Terfenol-D particles with a size of 0–300 μm. Slow mixing using a wooden stirrer was performed, followed by light brushing of the solution onto glass fiber prepregs. Distribution of these nanoparticles throughout the fibers was a quick step. After 24 h of refrigeration, the plies were then laid up for fabrication, and the fabricated samples passed through a magnetic field H in Tesla to align the magnetostrictive particles field. The fabrication procedure is shown in Figure 21.

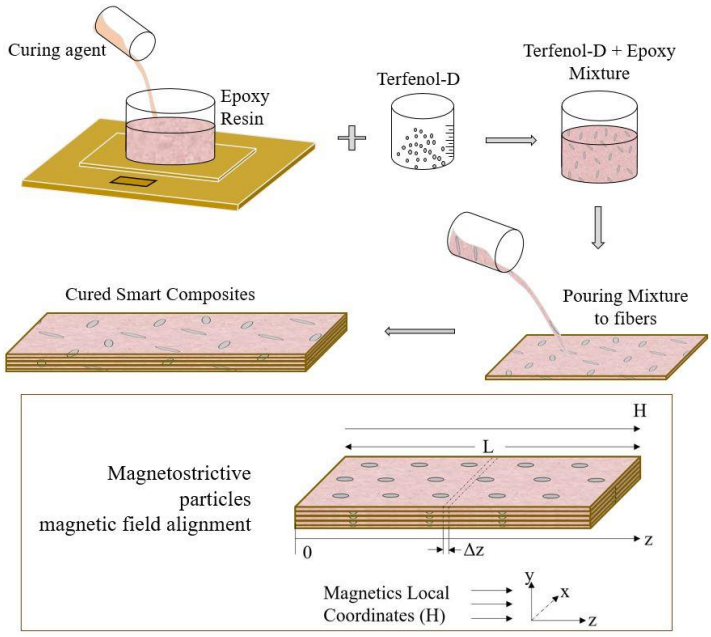

Figure 21. Fabrication procedure of smart self-sensing composites.

The reason these nanoparticles were selected is that Terfenol-D magnetostrictive alloy has a high magnetostrictive property in the range of 800–1200 ppm and a Young's modulus of 50–90 GPa. The presence of Terfenol-D particles within the composite contributed to the overall composite magnetic, electric, mechanical and thermal properties. This was therefore bound to change the composite stress–strain properties and damage modes within the system.

3.23. Compression Molding

Glass fiber unidirectional prepreg was selected for the composite used in this work. For all the samples tested, four plies of prepreg were cut into dimensions of 220 by 220 mm. All prepreg substrates were pre-weighted before fabrication. The first set of samples were of glass fiber-reinforced composite; the second set was of prepregs brush coated with the piezoelectric solution; the third set of samples were brush coated with the magnetostrictive solution; the last samples had both piezoelectric and magnetostrictive solution coatings. Two types of layups were conducted in this work: the first set of samples' layup orientation was 0° for all samples; the second set stacking

orientation was a 45°, −45°, −45°, 45° layup. The next step was placing the mold with the layup inside the compression molding chamber and moving it up towards the top mold. Before closing the chamber, the fabrication sequence was set with maximum compression pressure of 4 tons and a temperature of 275 °C. The chamber was then closed, and preheating started. The heating cycle for the glass fiber-reinforced composites was set for 48 min, in addition to a cooling cycle for 48 min with a cure time of 90 min. The mold and release layers were then peeled off the fabricated samples. The fabricated composite samples were then cut into specimens of dimensions 180 by 22 mm and taken for mechanical testing.

3.24. Detection System

The detection system used in this work for wireless detection of signals generated by the self-sensing smart magnetostrictive composite was based on the working principle of the transmitter and receiver antennas. Coupling of the two antenna coils with optimal detection response depends on various parameters, which include antenna coils design, coils dimensions, number of turns, and excitation signal type, amongst other parameters. The excitation and pickup coils in this work were of 0.025 mm^2 area and 1000 turns. Excitation frequency was at 50 kHz, and the magnetic field of 0.384 T was applied around the sensor system. The working principle of the detection system is based on electromagnetic coupling between the antenna coils and change in magnetization around the smart self-sensing composite due to the application of loading. Incident stresses/strains on the magnetostrictive self-sensing composite will give a reaction change in the magnetic field around the composite due to its Villari effect. This change in magnetization is used to characterize the generation of defects and defect precursors within the smart composite material, as shown in Figure 22.

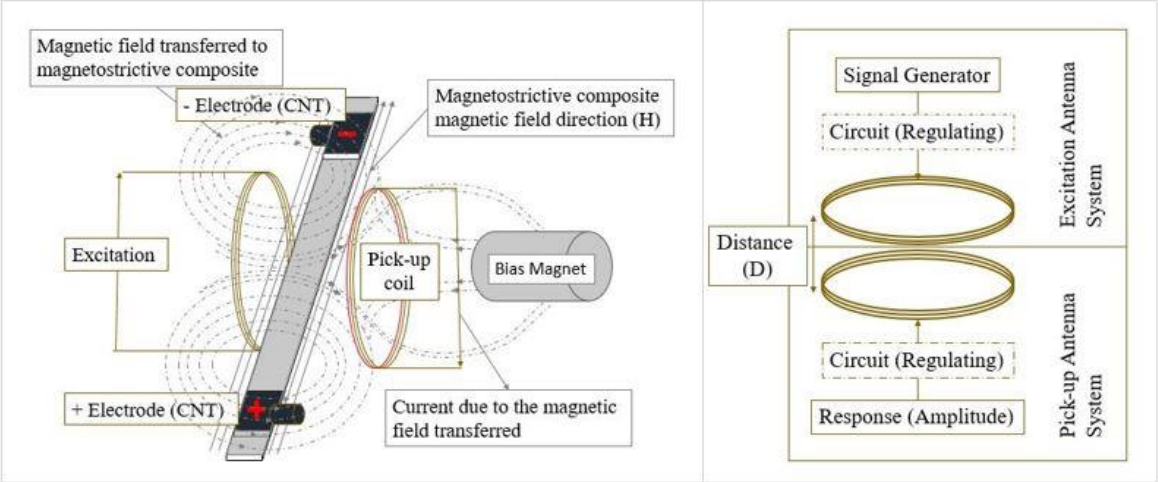

Figure 22. Working system of the designed magnetostrictive self-sensing smart composites detection system.

The detection system also entailed two electrodes at both ends of the composite. These electrodes were connected to an impedance analyzer, running voltage through the composite sample at 100 kHz frequency. The presence of a piezoelectric material within the composite sample will affect the collected voltage from the electrodes during mechanical testing as strain changes.

3.3. Results and Discussion

Characterization of the fabricated composite samples was conducted following different mechanical tests contributing to both piezoelectric and magnetostrictive responses for structural health monitoring. The distributed SWCNT morphology was examined using SEM working at 15kV. Figure 23a shows the single-walled carbon nanotubes forest before dispersion on fibers. Prepreg fibers coated with SWCNTs are shown in Figure 23b after SWCNT alignment. The image shows lesser agglomerations of pristine SWCNTs on prepreg fibers.

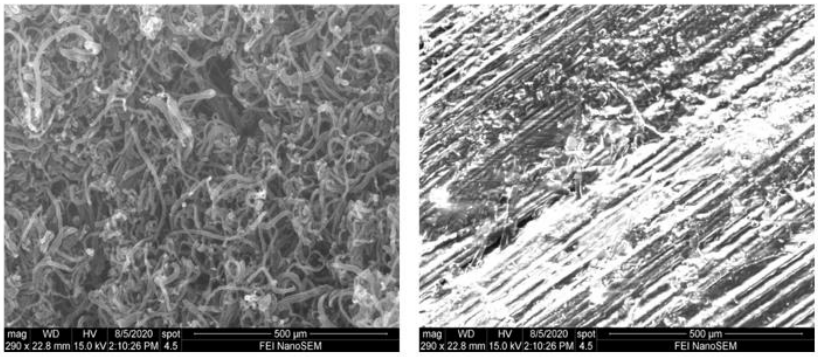

Figure 23. (a) SWCNT forest and (b) aligned SWCNT on prepreg glass fibers.

The variation of Terfenol-d alloy nano particles size was observed, and SEM images are shown in Figure 24, where Figure 5a shows the nanoparticles before chemical treatment and Figure 24b Terfenol-D nanoparticles after chemical treatment before dispersion on prepreg fibers. The size of the nanoparticles was found to vary from 0 to 300 µm.

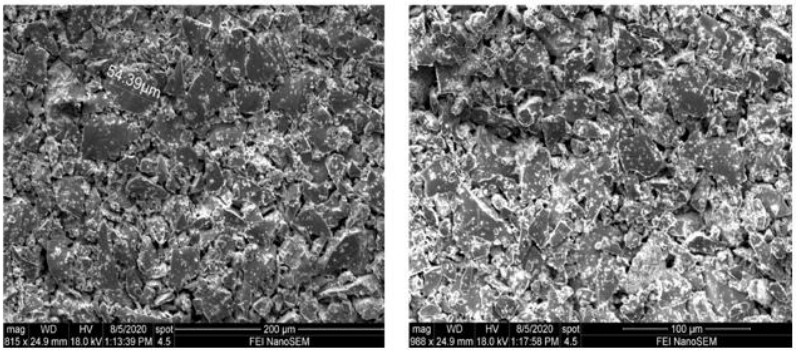

Figure 24. SEM images of (a) Terfenol-D nanoparticles before chemical treatment and (b) Terfenol-D nanoparticles after chemical treatment.

Nicolet 6700 FTIR Fourier transform infrared (FTIR) spectroscopy was used to determine the bonding characteristics of SWCNTs in prepreg samples. Thirty-two scans were collected for every sample. Several spots were targeted on the prepreg substrates coated with SWCNTs to determine

FTIR absorption peaks as shown in Figure 25. Absorption measurements were performed over wavelength ranging from 600 to 4000 cm^{-1}.

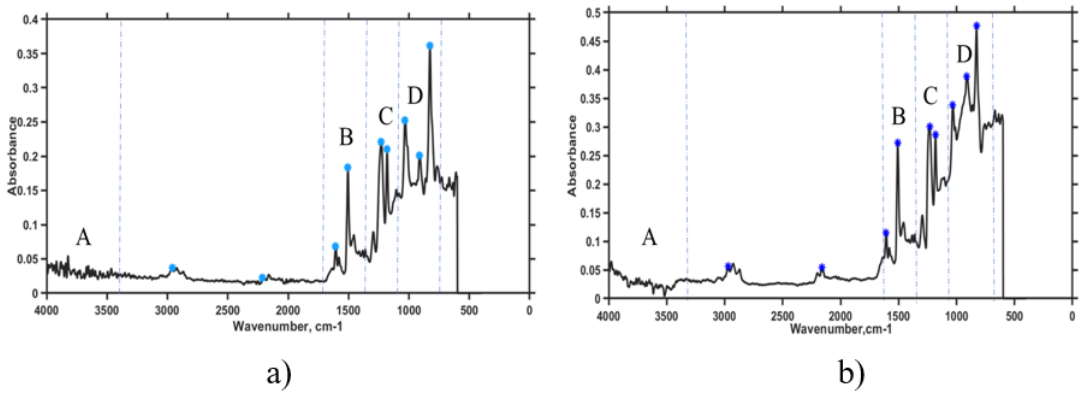

Figure 25. FTIR prepreg substrate SWCNT alignment characterization of samples (a) with no nanoparticles and (b) with Terfenol-D nanoparticles.

From FTIR analysis, it was found that the resin system in the prepreg contains diglycidyl ether of bisphenol-A mixture (DGEBA). The peak observed at 911 cm^{-1} in section D for both Figure 25 a,b confirm the presence of the epoxide group, which occurs due to the stretching of C–O. However, the oxirane group peaks at 2963, 1579 and 1505 cm^{-1} (section B) represent a benzene ring which is also constituent with DGEBA (1). A slight variation in absorption peaks for prepreg with Terfenol-D (Figure 25b) was observed due to the presence of isopropanol used in chemical treatment of these nanoparticles. The presence of SWCNT can be confirmed by the peaks at 1457 and 1606 cm^{-1} which correspond to SWCNTs. The FTIR analysis shows a slight deviation when adding magnetostrictive nanoparticles to the prepreg substrate with SWCNT. From the analysis, we determined that the peak broadening in Figure 25b at the 911 and 2200 cm^{-1} (sections B, C and D) wavelength corresponds to the epoxied group and nitrile. The peak boarding may occur because of the presence of a hydrogen bond. It was found that the dipole moment intensity of the epoxied group increased, which indicates less crosslinking. Both hardener and resin undergo hydrogen

bond reaction, which may cause a reduction of the C–O–C bond. Thus, Terfenol-D particles hinder the reaction between CNT and the resin system. The Terfenol-D particles also behaved like point defects or impurities in the prepreg system, which can also be a reason for peak boarding. These glass fiber-reinforced composite samples with aligned SWCNTs were passed through a series of quasi-static tensile tests to determine their overall contribution to the composite mechanical properties. The improvement of dielectric properties of the glass fiber-reinforced composite due to the presence of SWCNTs also enabled characterization of the sample's piezoelectric response. The SWCNT weight fraction was kept constant throughout this work based on literature studies [24]. A comparison of randomly dispersed SWCNTs and aligned SWCNTs was done, and the results are shown in Figure 26.

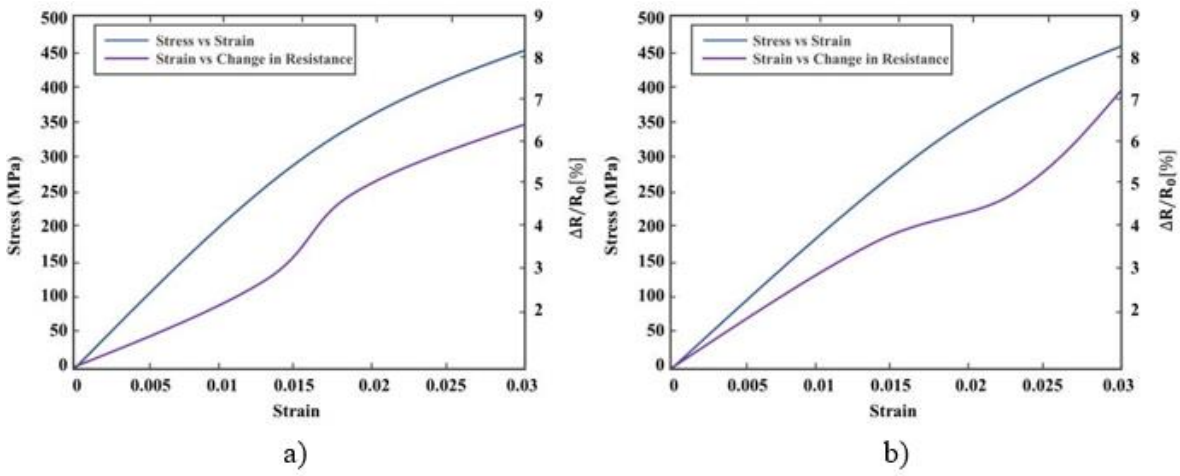

Figure 26. Glass fiber-reinforced SWCNTs: (a) non-aligned nanotubes and (b) aligned SWCNTs.

The comparison of electrical resistance change to strain was conducted for the SWCNT glass fiber-reinforced composite samples. Figure 26 shows a change in resistance for the strain results. Samples with aligned SWCNTs reached a maximum electrical resistance change of 7% as compared to non-aligned samples that increased to 6.4%. The sensitivity of non-aligned samples below strains of 0.013 was close to twice the sensitivity of aligned fibers below 0.013 strains, as

shown in Figure 27 a,b, respectively. A similar response was found in [25] where GFRP composite samples with sprayed-on CNT film were passed through a series of tensile tests monitoring the change in electrical resistance. Increase in tensile loading showed a linear change in electrical resistance below 0.015 strain. Minor defects generation above 0.015 strain affected the linearity of the electrical resistance change for both samples, showing a slight increase in slope and decline towards failure. This trend was also observed in [26], where piezoelectric properties of GFRP composites embedded with CNTs using different techniques were explored. Addition of Terfenol-D nanoparticles to the sample enabled the characterization of the Villari effect. This was achieved by comparing the change in voltage from the excitation coil as the magnetization around the composite sample changed with strains. The sensor dependence on the magnetic field applied is shown in the Section 3 (Experimental Methodology) and previous work [13]. Measurements were taken at room temperature using the SR860 Lock-in amplifier with AC excitation signal at 50 kHz. Sensor response repeatability was studied in [13], where the authors characterize cyclic loading of the composite sample at different loading rates. The detection device was observed to have consistent results with change in strain and generation of damage precursors. The response beyond composite failure lacked repeatability and, therefore, was not considered in this work. Linear amplitude response regression line gradient gave a standard error of 0.0035 (0.35%) with sensor resolution limited by the excitation signal and coil size. Different volume fractions of nanoparticles were studied in this work, and responses to strain were compared. Figure 8a shows the sample stress–strain responses for all volume fractions and Figure 8b the change in amplitude.

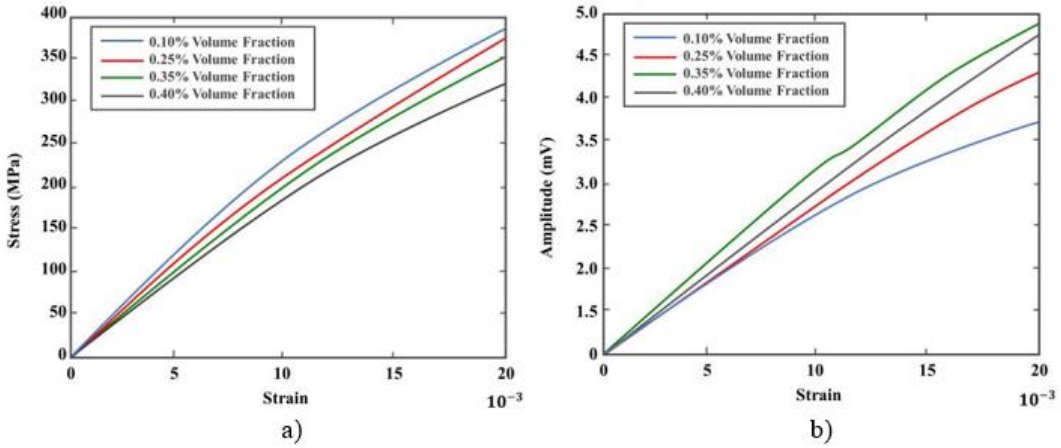

Figure 27. Composite with various volume fractions of SWCNTs: (a) stress–strain plot and (b) strain versus amplitude plot.

Composite samples with 0.35% volume fraction of Terfenol-D particles showed optimal change in the supplied voltage; therefore, this constituent ratio was selected for the fabrication of the self-sensing composite. Samples with Terfenol-d nanoparticles with a volume fraction greater than 0.35% reached their ultimate stress point quicker. From Figure 9a, it can be observed that the volume fraction of 0.10% has the highest modulus of elasticity of 22.94 GPa, but Figure 9b shows the lowest change in magnetization as per the amplitude change reaching a maximum of 3.6 mV. The volume fraction of Terfenol-D nanoparticle increase reduced the composite stiffness properties. Samples with the highest volume fraction of Terfenol-D nanoparticles had the lowest modulus of elasticity—0.40% volume fraction with the lowest overall slope, as displayed in Figure 8a. A similar trend was observed by Duenas and Carman in [27], where the increase in Terfenol-D volume fraction beyond 20% volume fraction affected their composite's stiffness properties. The increase in volume fraction of Terfenol-D also showed a direct increase in change in magnetization, which is reflected by the increase in picked-up amplitude (mV) shown in Figure 9b for samples with a volume fraction of 0.40% and 0.35%. The sample with the 0.35% volume fraction showed a higher change in amplitude, reaching its maximum at 4.8 mV, as shown in

Figure 8b. This increase in amplitude with the increase in Terfenol-D nanoparticles showed the dependency of the Villari sensing properties of the self-sensing composite on the Terfenol-D volume fraction. This was also observed in [28], where an increase in Terfenol-D nanoparticles caused an increase in the magnetic polarization.

Following the optimal combinations of constituents from both piezoelectric SWCNT tests and magnetostrictive Terfenol-D tests, a final type composite with both SWCNTs and Terfenol-D nanoparticles was fabricated and went through a series of quasi static tensile tests. The tests showed a low change in Young's modulus of the sample, as illustrated in Figure 28a,b by both the change in amplitude and electrical resistance. Both the change in amplitude and $\Delta R/R_0(\%)$ increased with increasing strain on the composite samples. At lower strains of 0.005, the magnetostrictive sensor showed a higher sensitivity of 290 mV/Ɛ and gradually decreased with increasing strains. The change in the electrical resistance gradient at strains below 0.02 was low and showed an increase in sensitivity from 3.8% to sample failure at a maximum stress of 420 MPa. The difference in change in electrical resistance shown in Figure 28b to that in Figure 28b is a reflection of Terfenol-d nanoparticles contributing to the overall composite electrical resistance.

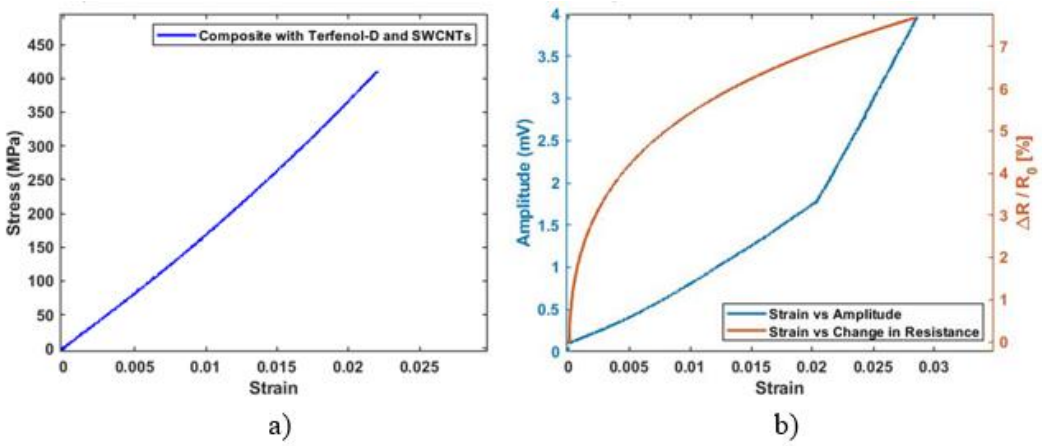

Figure 28. SWCNT/Terfenol-D composites: (a) stress–strain response; (b) amplitude response and change in electrical resistance.

The same linear relation at strains of 0.0017 in a composite with both SWCNTs and Terfenol-D was observed in the stress–strain plot compared to composite samples without any nanoparticles. Higher sensitivity at strains below 0.005 in the magnetostrictive sensor aligned with data from specimens that only had Terfenol-D nanoparticles, as shown in Figure 9b. This showed that the presence of SWCTs did not affect the magnetostrictive material response to strain. The composite Villari effect in the experimental work was affected by the size of the pickup coil, the distance between the composite sample and the pickup coil and the applied magnetic field. The variation of this parameters contributed to the experimental error. This is reflected by the difference in sensitivities, as shown in Table II. The difficulty in validation of the numerical model with experimental work was due to the differences in testing conditions of the simulation model, which include minor differences in fabricated composite samples and other environmental factors.

Table II. Comparison of experimental sensor sensitivity with COMSOL Multiphysics® data.

Specimen	Peak Stress (MPa)	Young's Modulus (GPa)	Sensitivity ($\mu V/\mu\varepsilon$)
GFRP Experimental	370	22.72	0.0457
GFRP/SWCNT Experimental	385	22.85	0.0543
GFRP/Terfenol-D Experimental	361	22.31	7.243
GFRP/SWCNT/Terfenol-D Experimental	366	22.51	6.495

The composite sample modelled in COMSOL Multiphysics® showed to have a better sensitivity than those in experimental work with the sample concentration of Terfenol-D

nanoparticles. The presence of Terfenol-D nanoparticles appeared to reduce the overall composite elastic modulus from 22.72 to 22.31 GPa. A slight increase in elastic modulus was observed with the addition of SWCNT, therefore proving to supplement the composite mechanical properties. From the experimental specimens, GFRP samples with Terfenol-D nanoparticles proved to have a higher sensitivity, which was slightly affected by the addition of SWCNTs, decreasing from 7.243 to 6.495 $\mu V/\mu\varepsilon$. The deviation of the modelled sensitivity value from the experimental sensitivity value might be the reason for the testing setup factors contributing to experimentation error as highlighted above. The next step of the tests was to determine how the fracture toughness of the composite was affected by the presence of both Terfenol-D nanoparticles and SWCNTs. This was achieved by exploring the delamination fracture toughness of the fabricated smart self-sensing composite. The resistance of the crack growth of the composite with applied strains is shown in Figure 10a, and strain energy release is shown in Figure 10b. Multiple samples with the same ratios of nanoparticles were tested and compared with samples without any nanoparticles. The crack propagation was dependent on the stress, the length of the initial crack and the geometric factor. This illustrates the relation of the stress intensity factor with fracture toughness. Crack propagation was found to be stable at low displacements of up to 5.4 mm (Figure 29a) equivalent to the strain of 0.034. Mode 1 crack is further explored through the plot, showing a drop in stress intensity factor as the crack becomes more unstable, and reduction in critical energy release rate is observed.

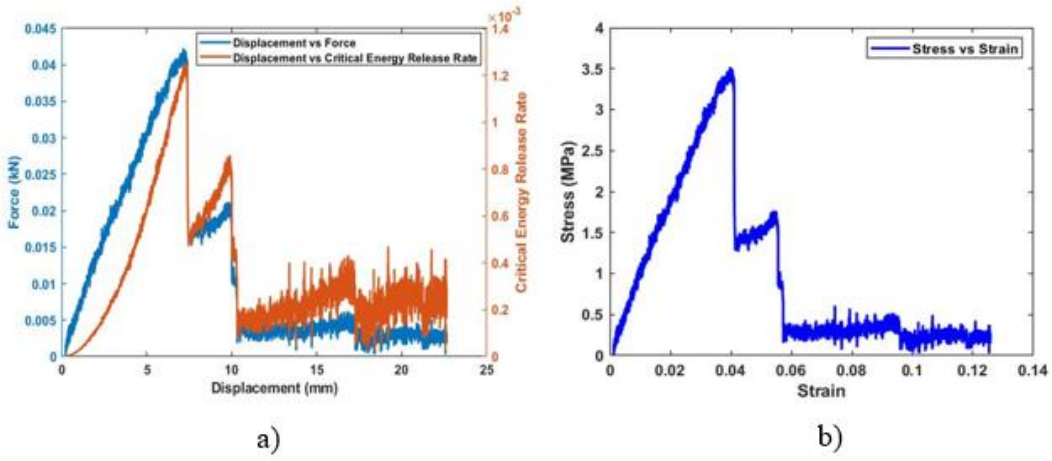

Figure 29. SWCNT/Terfenol-D composites: (a) force displacement and delamination plots; (b) critical strain energy release rate with change in displacement.

To further understand the mode 1 crack propagation for the fabricated smart self-sensing composite specimens, crack images were taken as delamination continued (Figure 30a), labeling the location of where the images were taken in relation to displacement force and the propagation of cracks through the composite images (Figure 30b).

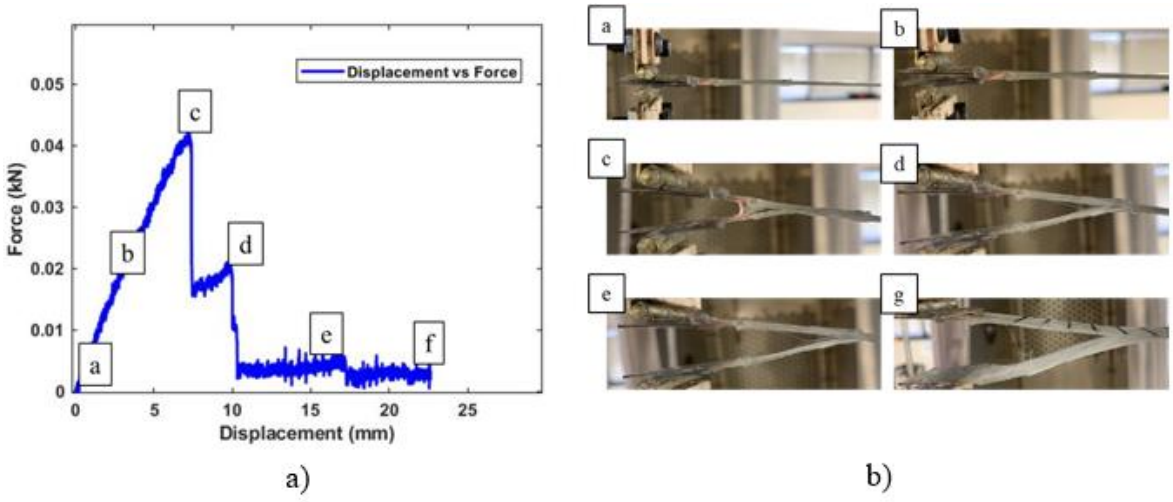

Figure 30. SWCNT/Terfenol-D composite: (a) delamination location on the displacement response curve and (b) crack propagation images.

The area under the stress–strain curve up to the point of fracture at maximum stress of 3.5 MPa shown in Figure 30b represents the toughness of the composite material. This is essentially the amount of energy that is required to break these SWCNT/Terfenol-D composite samples. In Figure 30a, the initial composite response to the applied load is shown in Image a, where the crack is still stable. Increase in load force opened up the initial prefabricated crack at Image b until it reached a point of fracture at 0.043 kN. This was observed to be a higher toughness as compared to similar samples in the literature [29,30]. Even though Terfenol-D particles may lead to reduced fracture toughness, the presence of SWCNTs improved the composite material resistance to crack propagation. The reduction of critical energy release rate shown in Figure 30a can now be observed in Figure 30b in Images c and d with an unstable crack propagation. The final stages, from crack tearing to complete failure, are shown in Images e and f.

3.4 Reference

[1] Light, G.M.; Kwun, H.; Kim, S.; Spinks, R.L. Magnetostrictive sensor for active health monitoring in structures. In Smart Nondestructive Evaluation for Health Monitoring of Structural and Biological Systems; International Society for Optics and Photonics: Bellingham, DC, USA, 2002; Volume 4702, pp. 282–288.

[2] Safri, S.N.A.B.; Sultan, M.T.H.; Jawaid, M. Damage analysis of glass fiber reinforced composites. In Durability and Life Prediction in Biocomposites, Fibre-Reinforced Composites and Hybrid Composites; Elsevier: Amsterdam, The Netherlands, 2018; pp. 133–147.

[3] Wang, H.R.; Long, S.C.; Zhang, X.Q.; Yao, X.H. Study on the delamination behavior of thick composite laminates under low-energy impact. Compos. Struct. 2018, 184, 461–473.

[4] Ciampa, F.; Mahmoodi, P.; Pinto, F.; Meo, M. Recent advances in active infrared thermography for non-destructive testing of aerospace components. Sensors (Switzerland) 2018, 18, 609.

[5] Rathore, D.K.; Prusty, R.K.; Kumar, D.S.; Ray, B.C. Mechanical performance of CNT-filled glass fiber/epoxy composite in in-situ elevated temperature environments emphasizing the role of cnt content. Compos. Part A Appl. Sci. Manuf. 2016, 84, 364–376.

[6] Yang, F.; Qian, S. Mechanical and piezoelectric properties of ecc with CNT incorporated through fiber modification. Constr. Build. Mater.2020, 260, 119717.

[7] Chen, S.; Luo, J.; Wang, X.; Li, Q.; Zhou, L.; Liu, C.; Feng, C. Fabrication and piezoresistive/piezoelectric sensing characteristics of carbon nanotube/pva/nano-zno flexible composite. Sci. Rep. 2020, 10, 1–12.

[8] Katabira, K.; Yoshida, Y.; Masuda, A.; Watanabe, A.; Narita, F. Fabrication of Fe-Co magnetostrictive fiber reinforced plastic composites and their sensor performance evaluation. Materials 2018, 11, 406.

[9] Na, S.M.; Park, J.J.; Jones, N.J.; Werely, N.; Flatau, A.B. Magnetostrictive whisker sensor application of carbon fiber-alfenol composites. Smart Mater. Struct. 2018, 27, 105010.

[10] Qhobosheane, R.G.; Islam, S.; Elenchezhian, M.R.P.; Vadlamudi, V.; Raihan, R.; Reifsnider, K.; Shen, W. Design of embedded wireless sensors for real-time and in-situ strain sensing of fiber reinforced composites. Struct. Health Monit. 2019, doi: 10.12783/shm2019/32238

[11] Sazonov, E.; Pillay, P.; Li, H.; Curry, D. Self-powered sensors for monitoring of highway bridges. IEEE Sens. J. 2009, 9, 1422–1429.

[12] COMSOL. The Structural Mechanics Module User's Guide; COMSOL: Stockholm, Switzerland, 2018.

[13] Rand, A.; Gillette, A.; Bajaj, A. Quadratic serendipity finite elements on polygons using generalized barycentric coordinates. Math. Comput. 2014, 83, 2691–2716.

[14] Sapra, G.; Sharma, P. Design and analysis of mems mwcnt/epoxy strain sensor using comsol. Pramana J. Phys. 2017, 89, 10.

[15] Sivakumar, N.; Kanagasabapathy, H.; Srikanth, H.P. Static multiple, distributed piezoelectric actuator structural deformation and bending analysis using comsol. Mater. Today Proc. 2018, 5, 11516–11525.

[16] Huang, W.; Deng, Z.; Dapino, M.J.; Weng, L.; Wang, B. Electromagnetic-mechanical-thermal fully coupled model for terfenol-d devices. J. Appl. Phys. 2015, 117, 17A915.

[17] Schwartz, T.J.; Alvandi-tabrizi, Y. Electric control of magnetization in biferroic heterostructures with patterned interfaces: A phase-field micromagnetic study. Available online: https://www.semanticscholar.org/paper/Electric-Control-of-Magnetization-in-Biferroic-with-Tabrizi/352c8dac341eca28c3a7a359e1a7b1e3a68a8cfc (accessed on 15 November 2020).

[18] Laksar, J.; Sobra, J.; Veg, L. Numerical calculation of the effect of the induction machine load on the air gap magnetic flux density distribution. In Proceedings of the 2017 18th International Scientific Conference on Electric Power Engineering EPE, Kouty nad Desnou, Czech Republic, 17–19 May 2017.

[19] Cao, Q.; Chen, D.; Lu, Q.; Tang, G.; Yan, J.; Zhu, Z.; Xu, B.; Zhao, R.; Zhang, X. Modeling and experiments of a laminated magnetostrictive cantilever beam. Adv. Mech. Eng. 2015, 7, 1687814015573761.

[20] Federico, S.; Consolo, G.; Valenti, G. Tensor representation of magnetostriction for all crystal classes. Math. Mech. Solids 2019, 24, 2814–2843.

Chapter 4: Detection of Damage Progression in Smart Self-Sensing Composite

4.1 Introduction:

During loading, composite materials are subjected to a variety of damage modes. The goal of this chapter is to correlate damage modes in fabricated smart self-sensing composites to data from structural health monitoring (SHM) detection devices. The voltage amplitude change picked up from a planar coil due to the magnetostrictive composite magnetization change during loading after voltage excitation and collection of dielectric data during composite loading are two SHM approaches employed in this chapter.

4.11 Damage Modes

The composites' strength and damage mechanisms are heavily reliant on the strength of the interphase, which is governed by the chemical and physical properties of its constituents. Damage in composite materials, its underlying mechanics, accumulation, and characterization, as well as the idea of damage tolerance, have all been investigated for more than three decades [1][2], but many of the fundamental concerns remain unresolved. The three basic failure modes of a composite are tension, compression, and shear. The projection of global loads onto the lamina major directions differs from lamina to lamina because the composite is made up of layers of varying orientations. The various stresses in the laminae rise as the load increases, and failure values can be reached in a single lamina in a single major direction without the total laminate failing; in other words, composite laminate failure is a gradual event [3]. For a time, this cumulative damage progression is subcritical, but it eventually leads to composite laminate collapse.

Intrinsic damage modes are damage modes that form within a lamina, as opposed to extrinsic damage modes that develop within a ply and between plies due to restrictions experienced by the plies of a laminate [4]. Fiber cracks, matrix yielding, matrix cracks, fiber-matrix interfacial debonding, and possibly fiber buckling are the numerous intrinsic damage processes in a UD lamina [5]. Due to a distribution in the tensile strength of the fibers, fiber cracking has been seen to begin at stresses as low as 40% of the [0]n laminate's tensile strength and gradually rise in number until final laminate failure during quasi-static loading [6]. During fatigue loading, matrix cracking and debonding, as well as progressive fiber cracking, were detected in the [0] lamina, as illustrated in Fig. 31 [7]. During quasistatic loading, however, no equivalent experimental observation of progressive matrix cracking or debonding prior to failure of a [90] or off-axis PMC lamina has been described. The final failure of these lamina is caused by the initiation and spread of a matrix crack, which can be caused by a fault or a fiber-matrix debond [8].

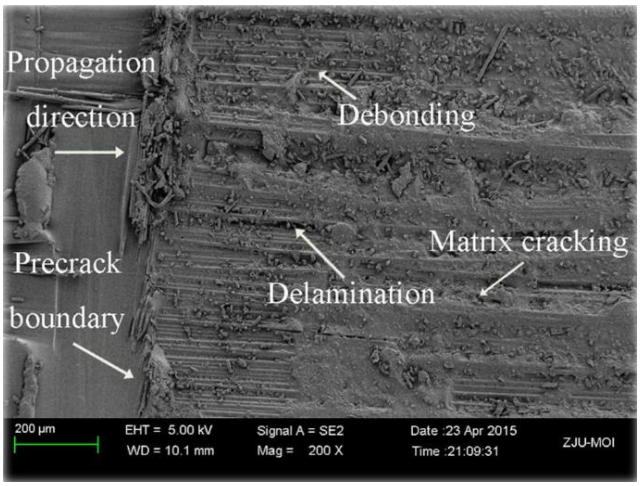

Figure 31. Composite damage and failures of carbon fiber/epoxy composite laminates under different loading raters [8].

Transverse fractures (also known as matrix cracks) that run parallel to fibers, delamination, vertical cracks, and fiber cracks in [0] plies of the MD laminate are examples of extrinsic damage modes that arise in an MD laminate.

4.2 Sample Fabrication

Four types of composite specimen were fabricated in this work for comparison of composite damage growth and correlation with sensor response. Glass fiber reinforced polymer (GFRP) composites specimen without nanoparticles were fabricated, GFRP with carbon nanotubes, GFRP with Terfenol-D nanoparticles and GFRP samples with both CNTs and Terfenol-D nanoparticles. All composite specimens were fabricated with both unidirectional glass fibers and woven fibers. Compression molding process was used for the fabrication the described composite samples using the WABASH MPI Genesis Four-Post (15 to 150 tons) Tool. In this press, pressing temperature, pressing time, and pressing speed can be controlled. To get good quality bubble-free composite specimen, a pressing procedure was developed. A square metallic frame of dimensions 24 inch × 24 inch and 1-ich thickness was used for the composites mold. A Teflon separating film was placed on each side of the frame to support the composite material and enabling separation of the sample from the mold plates. Four plies of fiber prepreg were placed between the release films for each specimen and nano particles were distributed following methods in [9]. The frame and plates were placed inside the hot press, and the press was closed so that both the hot-press plates (upper and lower) are in contact with the mold plates. The force on the press plates, during this time, is between 0 and 2 kN. The press is then opened by moving away the upper hot plate by a certain distance (4 mm), and then the press is again closed with the defined pressing speed. Temperature was ramped up at 3 °C/min from 21 °C to 135 °C, cured at 135 °C for 60 minutes, then cooled at 3 °C/min from 135 °C to 49 °C, as directed by the manufacturer. Cured panels were sliced into coupons according to ASTM D 3039[10]. For each of the stacking sequences outlined, a minimum of three samples were taken and tested.

4.3 Damage Progression with change in Magnetostriction

The present study examines the possibilities of incorporating nanomaterials into composite sheets as a non-invasive and non-destructive detection and assessment technique. The integrated sensor composite effectively becomes a smart structure with the ability to auto-detect damage by assessing material integrity in real time. Ferromagnetism has unpaired electronic spins that align parallel to each other in a region known as the domain. The domains are oriented randomly when the ferromagnetic material is not below external magnetic fields. When an external magnetic field is applied, electrons rotate with each other and become magnetized. Magnetostriction is a property of ferromagnetic materials which, when an external magnetic field is applied, the domains align with the external field, causing their to change shape or size during magnetization. For example, Terfenol-D, (Tb0.3Dy0.7Fe1.92) transforms into about 2000 micros trains in the 2 kOe field under mechanical strain [55]. Due to their high magnetic coefficient, Terfenol-D nanoparticles are an excellent candidate for the detection of damage in different types of polymer composites under different mechanical loading situations [11].

Ferromagnetic materials have proven useful as strain transducers in harsh-environment applications. Magnetostrictive materials such as Galfenol (Fe-Ga alloy), Alfenol (Fe-Al alloy), and Terfenol-D (Tb0.3Dy0.7Fe1.92) (TdVib, LLC., Ames, IA, USA) in a polymer composite are great candidates for embedded damage assessment of composite structures. In this study, magnetostrictive particles such as Terfenol-D were embedded in a composite structure, along with carbon nanotubes, to counter the damage in a composite system undergoing qausi static loading. The change in magnetization flux density as the applied load rose was detected using non-contact planar coils that monitored the change in excitation voltage inducing a sinusoidal magnetic field [12].

$$i(t) = I_e \sin \omega_e t \tag{3}$$

where I_e is the excitation current amplitude and ω_e is the angular frequency. The magnetic flux density can be calculated using the solenoid approach as,

$$\oint H \cdot dl = N_e I_e \sin(\omega_e t) \tag{4}$$

Where number of turns in the excitation coil are represented by N_e and using the magnetic flux we get,

$$B_{flux} = \frac{\mu^{\sigma} N_e}{l} I_e \sin(\omega_e t) \tag{5}$$

The magnetic flux passing through the magnetostrictive material is given as $\phi = B_{flux} A_{cs}$ where ϕ is the total magnetic flux and A_{cs} is the cross-sectional area. From Faraday's law of induction, the voltage in the open-sensing coil is given by $V_o(t) = N_s(d\phi(t)/dt)$ where N_s is the number of turns in the sensing coil [13]. By substitution of the magnetic flux into the voltage equation, the sensing output voltage is given by,

$$V_o(t) = \frac{\mu^{\sigma} N_e N_s A_{cs}}{l} \omega I_e \cos(\omega_e t) \tag{6}$$

A change in the magnetic characteristics of the composite acted as an indicator of early-stage damage detection, according to several experiments.

4.4 Measurement Under Tensile Loading

The four types of composites fabricated were investigated: glass fiber reinforced polymer (GFRP) composites and glass fiber reinforced polymer (GFRP) composites with single walled carbon nanotubes (SWCNT), GFRP composites with Terfenol-D nanoparticles and GFRP composites

with both SWCNT and Terfenol-D nanoparticles. Each type was tested under uniaxial tensile loading using an MTS Servo-hydraulic test system, and the planar coils placed close to the composites were used to send the excitation signal and pick up the magnetic flux change at the sensor during the tensile loadings, as shown in Figure 32. The sample size was 14 × 1 cm. Discrete measurements and continuous measurements were both taken during uniaxial tensile loadings. For the discrete measurement, a tensile load was applied at three different load levels: 2 kN, 4 kN and 6 kN. At each of these three load levels, sensor measurements were taken over frequencies ranging from 0 Hz to 5 kHz. The continuous measurements were taken at 50 kHz and 100 kHz up to 4 kN, which was below the breaking load of most composite coupons.

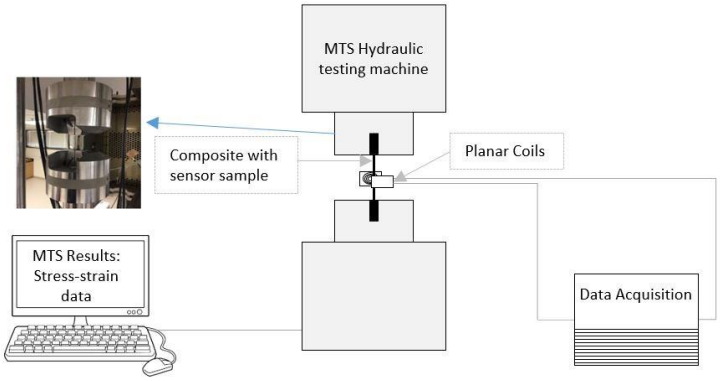

Figure 32. A schematic of the experimental set-up for sensor measurement during tensile loadings.

4.5 Imaging Methodology

The composite samples in this work were examined with the hirox microscope to achieve the image resolution required. The replica technique used involved softening an acetate tape in acetone, applying it to the composite surface, and then allowing it to harden as acetone evaporates. After careful removal from the surface, the acetate tape contains a negative image, or replica, of the composite surface that can be directly examined. These steps were done during tensile loading

of the sample from 0 loading to 1 kN, a 60 seconds break was taken for imaging. Tensile loading was then continued for another 1 kN to 2kN. After this, loading was paused for 60 seconds and the replication process repeated. This was done for multiple intervals until the composite failed. Double-faced tape was used to bond the replica to the glass slide to obtain large, flat, undistorted replica surfaces. The advantages of this process include getting a permanent record of the specimen is obtained, better resolution and higher magnification can be used, and contamination of the polished surface is minimized.

4.6 Damage Progression During Testing

This section gives details of all the experimentations done in this work to characterize the properties of the smart self-sensing composite. The change in properties of the composite structure is also relayed in this section. First the mechanical tests were done on the GFRP samples, then samples with SWCNT, samples with Terfenol-D and finally samples with both SWCNT and Terfenol-D nanoparticles as shown in Figure 33.

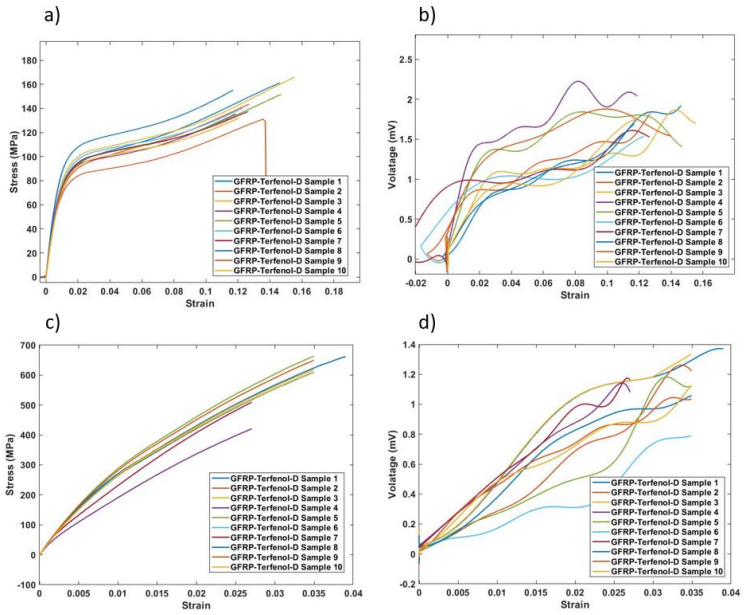

Figure 33. GFRP-Terfenol-D composite a) stress strain for +-45 orientation composite, b) sensor response for -+45 orientation composite, c) stress strain for 45, 90, -45, 0 orientation and d) sensor response.

During tensile loading, fiber layers are forced to separate from the matrix causing the delamination between plies and matrix and intralaminar cracks. The next study was to investigate the response of the composite embedded nanoparticles as defects develop within a composite sample. The composite permittivity change was monitored for all samples. The change in magnetization for all samples was also monitored following the excitation and pickup technique developed in previous works giving the collection of voltage change. This change as crack propagates was related to the development of defects within the composite. The response of the GFRP – Terfenol-D composite sensor data during continuous tensile loading is shown in Figure 34 with edge replicas of all defects.

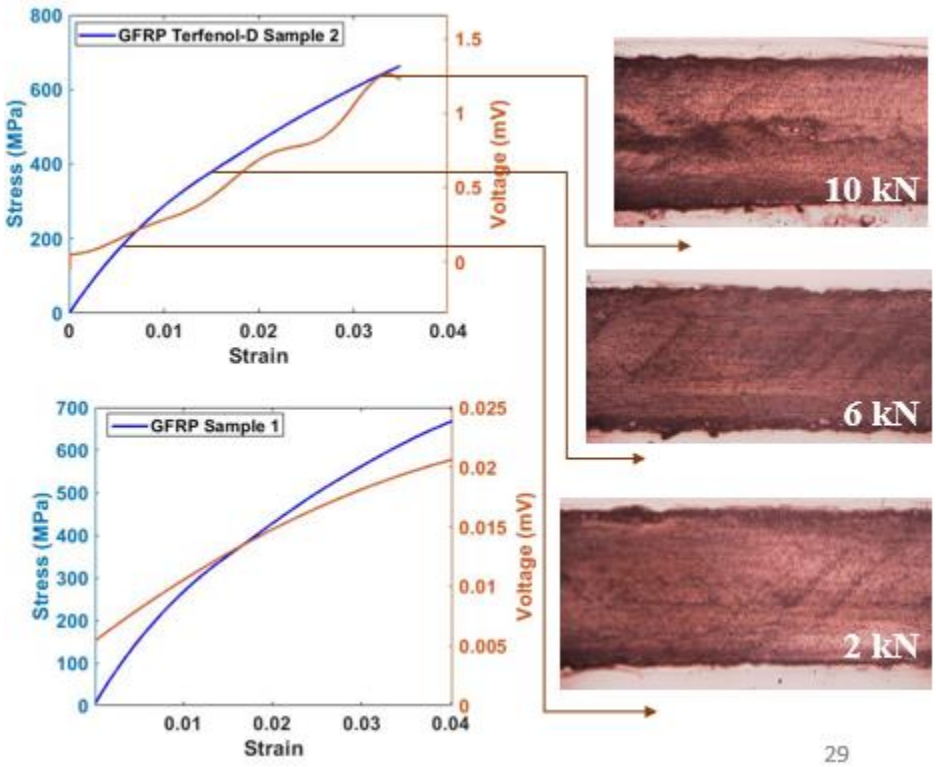

Figure 34. GFRP-Terfenol-D load response with respect to strain and voltage response resulting in generation of damage modes.

The initial voltage change for GFRP-Terfenol-D is shown in Figure 34 as a function of strain. The voltage change of the GFRP-Terfenol-D composite ranged from 1 mV to 1.5 mV. It should be noted that the sensor response gradually increased in proportion to increasing tensile load on the composite sample. The sensor output voltage increases linearly with load but shows a very low change in voltage for GFRP without magnetostrictive Terfenol-D nanoparticles as shown in Figure 35. Increase in loading resulted in generation of defects within the composite shown in Figure 35 and still slight increase in voltage response.

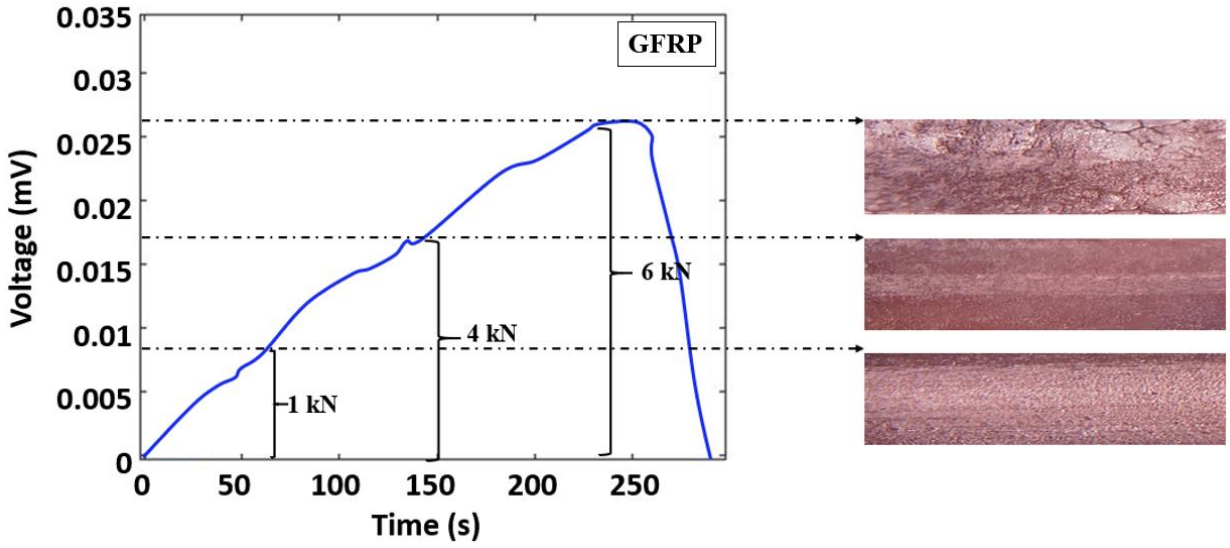

Figure 35. GFRP sensor voltage response during loading and edge replica images.

The development of defects within the composite during tensile loading were imaged using replicating tape and Hirox microscope. A similar experimentation was done for composite samples embedded with SWCNT. Figure 36 shows the response of the composite embedded with SWCNT during continuous tensile loading. Figure 36 shows no defects at initial loading. As loading increases with the voltage response, the development of cracks is noticed. Figure 36 show the GRFP-SWCNT structure still intact at initial loading. The load graphs showed a linear distribution in Figure 36, as time and force increase. It is seen that the composite experiences a brittle fracture

showing linear deformation at low and high loadings. Increase in loads applied on the composite sample to 2kN resulted in the development of minor cracks in the composite shown in Figure 36. The development of defects within the composite shows a slight increase in voltage response.

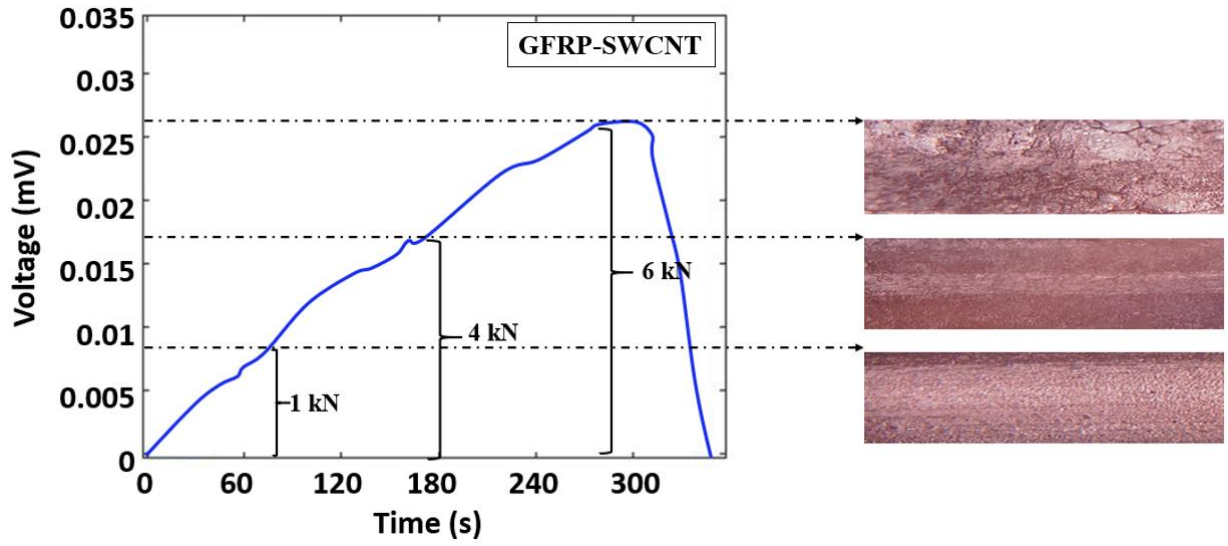

Figure 36. GFRP-SWCNT sensor voltage response during loading and edge replica images.

Further loading of the GFRP composite resulted in the propagation of these minor defects into cracks shown in Figure 36 at 6 kN loading within the composite. The development of cracks results in less increase in voltage response as the composite sample did not have any magnetostrictive material within it. GFRP-Terfenol-D composites loading response showed a trend like that of GFRP composite. The difference is observed from the peak loading. These composite samples with Terfenol-D nanoparticles showed a voltage response of higher sensitivity from initial loading to composite failure. Figure 37 shows the distribution of defects for this composite sample resulting in cracks of bigger sized compared to those of GFRP samples. Imaging of the GFRP-Terfenol-D composites at initial loading did not show any defects due to loads. Increase in loads on the samples resulted in steepness of the voltage response increase at a higher rate in turn defects leading to the development of matrix cracks were observed as shown in Figure 8 from 2 kN to 4

kN. At high loads, GFRP-Terfenol-D composite showed a decrease in sensitivity as deeper cracks develop within the structure shown in Figure 37 peak response.

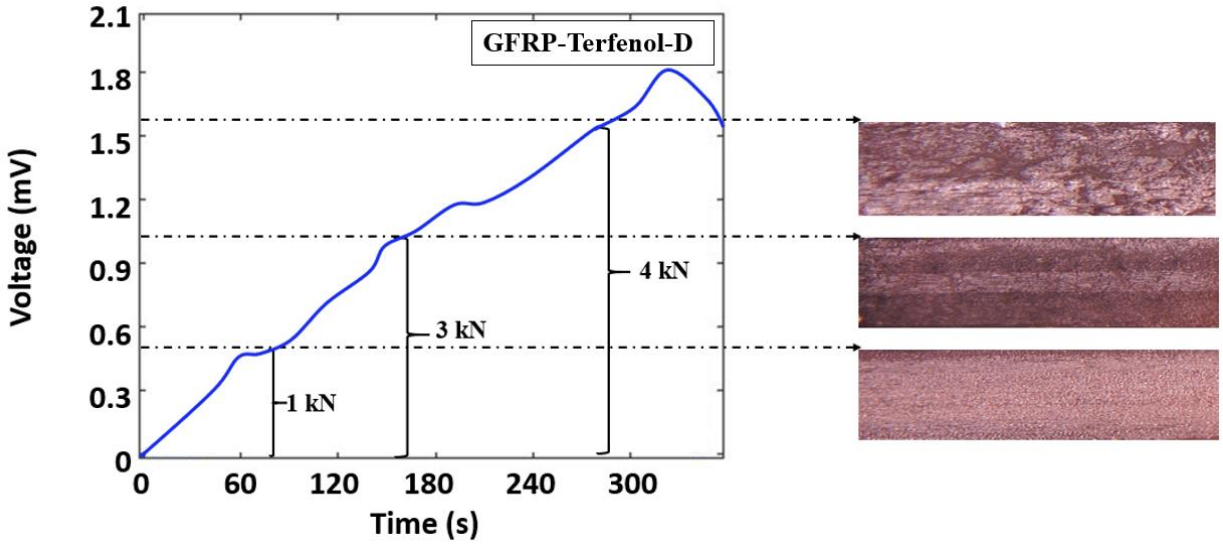

Figure 37. GFRP-Terfenol-D sensor voltage response during loading and edge replica images.

An increase in slope of the voltage response is observed with increase in loading. The size of cracks developed on the composites structured increases with increase in loading until the composite failed at peak load. Finally, the same experimentation was done on the SWCNT and Terfenol-D nanoparticles composite sample. With further increase in loading, the sensor output voltage shows a considerable non-linear increase. This irregularities in sensor output were attributes of different elastic properties of the GFRP-SWCNT-Terfenol-D composite. It is shown that the specimen exhibits an average peak voltage value of 1.69 mV.

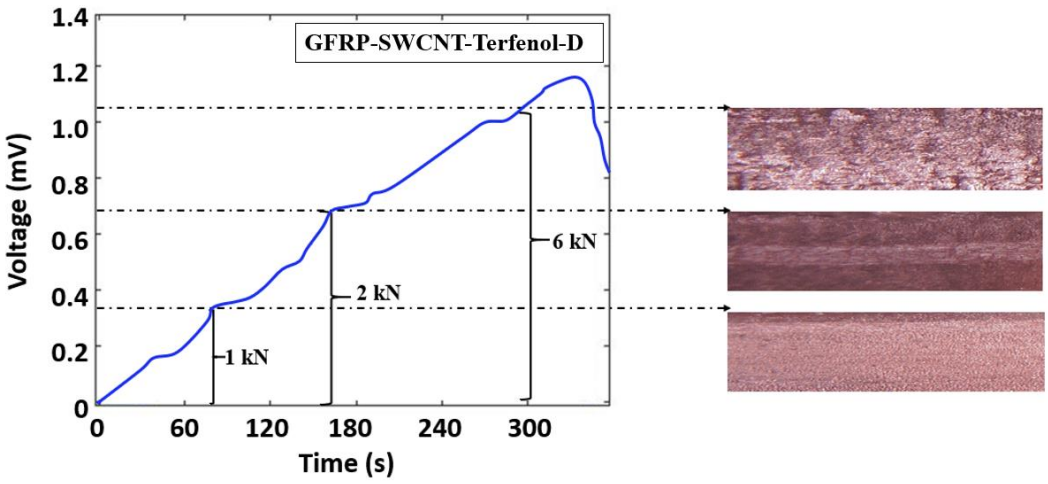

Figure 38. GFRP-Terfenol-D sensor voltage response during loading and edge replica images.

The sensor voltage response at low loading increases linearly with load and on further loading, the slope of the sensor voltage response decreases at peak after crack of the composite samples as shown in Figure 38. The sensitivity shown by the GFRP-SWCNT-Terfenol-D composite is 5.7 μV/με for the measurement at 100 kHz.

4.7 References

[1] Ao Zhou, Qiwen Qiu, Cheuk Lun Chow & Denvid Lau. "Interfacial performance of aramid, basalt and carbon fiber reinforced polymer bonded concrete exposed to high temperature." Composites Part A: Applied Science and Manufacturing 131.105802 (2020).

[2] B.Kim, H. Doh, K.Yi & Y. Lee. "Effects of structural fibers on bonding mechanism changes in interface between GFRP bar and concrete." Composites Part B: Engineering 45.1 (2013): 768-779.

[3] D. Xu, P. F. Liu, Z. P. Chen, J. G. Li, J. X. Leng, R. H. Zhu, L. Jiao, J. Mu, Y. Y. Li & L. L. Wang. "Delamination Analysis of Carbon Fiber/Epoxy Composite Laminates Under Different Loading Rates Using Acoustic Emission." Journal of Failure Analysis and Prevention 19 (2019): 1034–1042.

[4] D3039/D3039M-08, ASTM. "Standard Test Method for Tensile Properties of Polymer Matrix Composite Materials." ASTM Compass 15.03 (2014).

[5] Dhiraj Kumar, K. K. Singh & Redouane Zitoune. "Experimental investigation of delamination and surface roughness in the drilling of GFRP composite material with different drills." Advanced Manufacturing: Polymer & Composites Science 2.2 (2016): 47-56.

[6] Gemi, Emrah Madenci. Yasin Onuralp Özkılıç & Lokman. "Experimental and theoretical investigation on flexure performance of pultruded GFRP composite beams with damage analyses." Composite Structures 242 (2020).

[7] Jianglin Li, Zihua Mai, Jianhe Xie & Zhongyu Lu. "Durability of components of FRP-concrete bonded reinforcement systems exposed to chloride environments." Composite Structures 279.114697 (2022).

[8] Kenichi Katabira, Hiroki Kurita, Yu Yoshida and Fumio Narita. "Fabrication and Characterization of Carbon Fiber Reinforced Plastics Containing Magnetostrictive Fe-Co Fibers with Damage Self-Detection Capability." Magnetoelastic Sensors 19.22 (2019).

[9] Kenya Nakajima, Shota Tanaka,Kotaro Mori,Hiroki Kurita & Fumio Narita. "Effects of Heat Treatment and Cr Content on the Microstructures, Magnetostriction, and Energy Harvesting Performance of Cr-Doped Fe–Co Alloys." Advanced Engineering Materials (2021).

[10] Lei Chen, Yao Wang, Tianhong Luo, Yongkang Zou, and Zhongjie Wan. "The Study of Magnetoimpedance Effect for Magnetoelectric Laminate Composites with Different Magnetostrictive Layers." Materials 14.21 (2021).

[11] Relebohile George Qhobosheane, Muthu Ram Prabhu Elenchezhian, Partha Pratim Das, Minhazur Rahman, Monjur Morshed Rabby, Vamsee Vadlamudi, Kenneth Reifsnider, Rassel Raihan. "Smart Self-Sensing Composite: Piezoelectric and Magnetostrictive FEA Modeling and Experimental Characterization Using Wireless Detection Systems." Sensors 20.23 (2020): 6906.

[12] Sreenivasulu, Reddy. "Optimization of Surface Roughness and Delamination Damage of GFRP Composite Material in End Milling Using Taguchi Design Method and Artificial Neural Network." Procedia Engineering 64 (2013): 785-794.

[13] Srinivasu Dasari, Shiny Lohani, Soumya Sumit Dash, Abhinav Omprakash Fulmali, Rajesh Kumar Prusty & Bankim Chandra Ray. "A novel study of flexural behavior of short glass fibers as secondary reinforcements in GFRP composite." Materialstoday Proceedings 47.11 (2021): 3370-3374.

[14] Y.Lee, B.Kim &. "Resistance of interfacial debonding failure of GFRP bars embedded in concrete reinforced with structural fibers under cycling loads." Composites Part B: Engineering 156 (2019): 201-211.

[15] Yang Shi, Ni Lia, Yongkun Wang & Junjie Ye. "An analytical model for nonlinear magnetoelectric effect in laminated composites." Composite Structures 263.113652 (2021).

Chapter 5: Finite Element Analysis of Smart Self-Sensing Composite

5.1 Introduction:

The development of non-destructive structural health monitoring techniques has gained popularity in recent years[1]. This has led to the rise of different SHM methods which include magnetostrictive sensors. Magnetostriction is the property of a ferromagnetic material that enables it to change in shape in the presence of a magnetic field[2]. This property is used in the development of SHM sensors to study the development and propagation of defects in materials. Structural health monitoring sensors work on the principle of reverse magnetostriction of magnetostrictive materials. This is the change in magnetization around a ferromagnetic material due to the application of strain. This phenomenon is known as the Villari effect of a material[3]. This work contributes to a continues study from [4] which focuses on the development of magnetostrictive sensors for structural health monitoring. The focus of this work is on the development of a finite element method (FEM) model for a magnetostrictive sensor used to investigate defects within a carbon fiber reinforced polymer (CFRP) composite material. The numerical analysis is compared with experimental data demonstrating areas of improvement.

There are different models used to analyze the magnetostrictive material properties and forces coupling which include, Gibbs free energy-based model, Amstrong model, a Preisach based phenomenological model and a Thermodynamic approach[5]. Gibbs free energy (G) [6] based model imposes linear constraints on the system based on the first laws of thermodynamic. This is a thermodynamic state function dependent on the system imposed electrical field, magnetic field, gravitational field, pressure and temperature. G. Nicholas [7] demonstrated the implantation of the Gibbs free energy-based model in a giant magnetostrictive materials (GMM) FEM model development. From the 3D nonlinear model, feasible performance predictions and design

optimization of the GMM was detailed. Amstrong model is a nonlinear magnetomechanical constitutive energy-based model used to couple magnetostriction and magnetic permeability. This model includes the dynamic behavior and nonlinear properties of magnetostrictive materials demonstrated by U. Ahmed [8] in the FEA analysis of a magneto-mechanical energy harvesting based on giant magnetostrictive materials (GMMs). A Preisach based phenomenological model is a method that gives the sum of a distribution of ideal hysterons entailing the non-real, a real and ferroic material description. The incorporation of iron losses in the finite element method for accurate predictions of the performance of low-frequency electromagnetic device by implementation of the classical Preisach model was illustrated by Sajid Hussain [9]. This model proved to compute the desired results when compared against the conventional implementation.

COMSOL Multiphysics commercial software [10] was used in this work for ease of mechanical forces, electrical and magnetic forces coupling. Ideal modeling of composites and sensors relies on the accuracy of the numerical analysis in predicting the structural properties. Different works have illustrated numerical experimentations on composite structures using COMSOL Multiphysics[11]. This include V. Antonucci[12] is work illustrating the mechanical response of a composite structure due to the application of an indentation force. As accurate as the numerical data can be, this work proved how differences in experimental and numerical data may be observed due to fiber lay-up, orientation or other experimental factors. COMSOL Multiphysics can couple different physics in one structural model. This work[13] demonstrated how thermodynamics parameters interact with the electrical parameters in modeling of the resistance welding process. For the development of complex composite structures, T.Y.Sun [14] proposed a method of coupling the magnetic and electrical properties of the structures to determine the magnetostrictive

and piezoelectric coefficients. This COMSOL iteration proved to output results in close agreement with literature data.

The model developed in this work involves complexities of different multiphysics. A carbon fiber reinforce structure with an imbedded magnetostrictive sensor involved both the induction of magnetization properties coupled with the solid mechanics physics. Excitation and pickup coils introduced the field domains physics. The interaction of the magnetostrictive material with the composites strains was modelled using its Villari effect which according to Le Chatelier"s principle[15] can be related by,

$$\left(\frac{d\lambda}{dH}\right)_{\sigma} = \left(\frac{dB}{D\sigma}\right)_{H} \qquad [1]$$

Where the flux density is given by B and changes due to the variation of stresses represented by σ in the presence of a magnetic field H. This principle is therefore used to numerical characterize the strains within the composite material due to the application of forces.

5.2 COMSOL Model Development

This section gives detailed steps followed in the development of the COMSOL model for the glass fiber composite embedded with Terfenol-D sensors. A stationary study was done to illustrate quasi-static experimentation parameters. The first step was to model the composite without any sensor material to establish a base study for this work. This was followed by modeling of a more complex unit cell model entailing the sensor material and detection setup.

5.21 System Model

The next step in numerical analysis was the development of the composite embedded with nanoparticle model coupled with the sensor excitation and detection systems. The model was in

2D space with magnetic fields, solid mechanics, electric and magnetostrictive physics analysis using a stationary solver. The model was developed for a composite with glass fiber, Terfenol-D particles and single-walled carbon nanotubes (SWCNTs). The materials used in this system with their properties include those given in Table I.

Table I. Materials used on the COMSOL Multiphysics® model and their properties.

Property	Unit	Glass Fiber	SWCNT	Terfenol-D
Density	g/cc	2.44	1.9	9.25
Modulus of Elasticity	GPa	72.4	34.65	50–90
Thermal Conductivity	W/(m-K)	1.3	3500	13.5
Electrical conductivity	S/m	1.05×10^{-4}	10^{6}–10^{7}	1.6667×10^{6}
Poisson's ratio	-	0.20	0.311	0.4
Relative Permeability	-	1–4.5	100.3	2–10
Linear Magnetostriction	ppm	-	-	800–1200

5.22 Geometry

The geometry of the device structure is symmetric, therefore enabling single quadrant modeling in COMSOL. The sensors consist of a circular shape coils and a composite unit cell of Terfenol-D magnetostrictive material centered within the composite matrix with two fibers and carbon nanotubes on the side. Planar and excitation homogenized multi-turn coils of 1000 turns of circular geometry were on both sides of the composite. To prepare for the implementation of COMSOL physics, coupling components and geometry selections were done. Integration parameter for the

points of maximum deflection during loading and an average operator were used. The geometry for the overall system is shown in Figure 36.

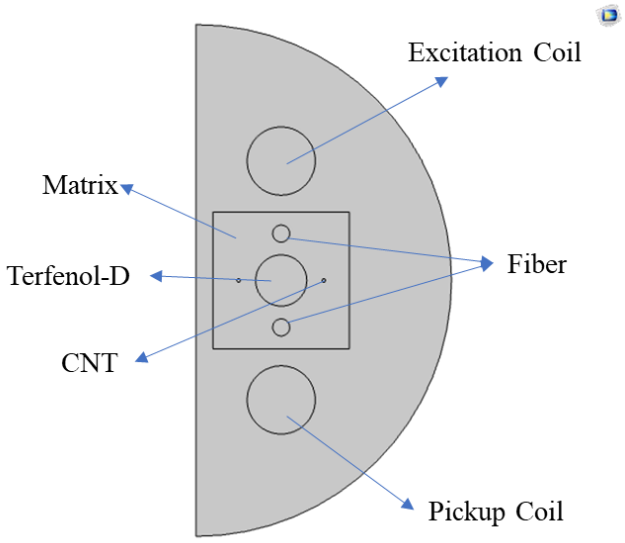

Figure 36. Smart self-sensing composite unit cell with two coils excitation and pickup coil.

5.23 Physics

A layer of air was defined around the system to mimic infinite volume domain. Boundary conditions and scaling conditions were set for this model to enable accurate loading properties. The air boundary layer surrounded the sensor composite structure. The first step in the development of the composite mechanics properties was to characterize the force equilibrium by Navier's equation[18],

$$-\nabla \cdot \sigma = F \qquad [2]$$

Where the volume force is represented by F and the stress tensor given by σ. The stress tensor vector is therefore given as $\sigma = [\sigma_{xx}\ \sigma_{yy}\ \sigma_{zz}\ \tau_{xy}\ \tau_{xz}\ \tau_{yz}]^T$ resulting in two equation of force balances in r and z directions[19][18].

$$\frac{\partial \sigma_r}{\partial r} + \frac{\partial \tau_r}{\partial r} + \frac{\sigma_r - \sigma_\theta}{r} + F_r = 0 \quad [3]$$

$$\frac{\partial \tau_{rz}}{\partial r} + \frac{\partial \sigma_z}{\partial r} + \frac{\tau_{rz}}{r} + F_z = 0 \quad [4]$$

The added τ accounts for the off-diagonal strain or shear components in the composite system during loading. The stress strain relation is therefore developed using the plane strain equation given as,

$$\begin{bmatrix} \sigma_x \\ \sigma_y \\ \sigma_z \end{bmatrix} = D\left(\begin{bmatrix} \varepsilon_x \\ \varepsilon_y \\ \varepsilon_z \end{bmatrix} - \alpha \begin{bmatrix} T - T_{ref} \\ T - T_{ref} \\ T - T_{ref} \end{bmatrix}\right) \quad [5]$$

Where $\varepsilon_x, \varepsilon_y, \varepsilon_z$ and γ_{xy} are components of the strain tensor, T the operating temperature, T_{ref} the reference temperature, α is the coefficient of thermal expansion and D is given as,

$$D = \frac{E}{1 - v^2} \begin{bmatrix} 1 & v & 0 \\ v & 1 & 0 \\ 0 & 0 & \frac{1 - v}{2} \end{bmatrix} \quad [6]$$

Where E is the Young's modulus and v represents the Poisson's ratio. The strain relation to displacement of the sensor composite was given by,

$$\varepsilon = \frac{1}{2}(\nabla u + \nabla u^T) \quad [7]$$

Where u is the displacement vector given as u = (u, v, w) in all possible directions and T as the stress tensor. Multiplying equation (2) by test vector u and integrating over the sensor composite domain (Ω) results in the weak form of Navier's equations[18] given as,

$$\int_\Omega u \cdot (-\nabla \cdot \sigma - F) d\Omega = 0 \quad [8]$$

Where vector $\nabla \cdot \sigma$ after divergence of a tensor given as,

$$\nabla \cdot \sigma = \begin{bmatrix} \frac{\partial \sigma_{xx}}{\partial x} + \frac{\partial \sigma_{xy}}{\partial y} + \frac{\partial \sigma_{xz}}{\partial z} \\ \frac{\partial \sigma_{yx}}{\partial x} + \frac{\partial \sigma_{yy}}{\partial y} + \frac{\partial \sigma_{yz}}{\partial z} \\ \frac{\partial \sigma_{zx}}{\partial x} + \frac{\partial \sigma_{zy}}{\partial y} + \frac{\partial \sigma_{zz}}{\partial z} \end{bmatrix} \quad [9]$$

Using the Green's formula [20][18] and substitution of stress and traction therefore gives the Navier's equation as,

$$-\int_{\partial\Omega} \sigma(u) n \cdot v ds + \int_{\Omega} \sigma(u) : \left(\frac{1}{2}(\nabla u + \nabla u^{T})\right) dx = \int_{\Omega} F \cdot u dx \quad [10]$$

The deformations are distributed through the composite to the sensor material embedded within the composite. Scaling of the degrees of freedom controlled the displacement limits of the entire system. These were related to the selected physics for each component of the model. Lagrange shape functions [21] were selected for all systems to enable smooth coupling of multiphysics and conventionality in displacement shape functions. To define the individual material properties, blank materials were added, and properties set as given in the materials section above. Each material was linked to a specific component in the system. The circular domain of the copper coils was selected within the magnetic field domains with current excitation modelled by Maxwell's equations [22][23].

$$\nabla \times H = J + \frac{\partial D}{\partial t} \quad [11]$$

Where, H is the magnetic field intensity, J is the current and D the electrical displacement field. The sensor composite was in the presence of magnetic fields and to model the magnetic and electrical fields interface, magnetic vector potential[24][19], A is solved as,

$$\nabla \times (\mu^{-1}\nabla \times A) = J_s \quad [12]$$

The magnetic vector potential can therefore be characterized as $B = \nabla \times A$. Loading constraints were specified for the composite material to achieve tensile loading of the composite embedded with a sensor. The loads on the fiber reinforced composite were defined on a point. In COMSOL, points have no area therefore this enables infinite stresses. This resulted in high stresses around the midpoint area due to the stress singularity. The size of this area was controlled by the mesh size and material properties. The generated mechanical stresses in the fiber reinforced composites resulted in strains distributed to the magnetostrictive material embedded within the composite. This contributed to the change in magnetization around the sensor. Magnetic field physics was used to create magnetic field domains around the sensor material amplifying magnetization. The field magnetic domains are of the same magnitude resulting in multidirectional magnetization represented by the direction vector m. COMSOL requires these parameters to enable characterization of the magnetostrictive material Villari effect[25]. Directional cosines β_i were used to define the sensor strains[26][19] in any direction as,

$$\lambda = \frac{\Delta l}{l} = \sum_{i,j} \beta_i \beta_j \, \varepsilon_{ij} \quad [13]$$

From this, the magnetostrictive strain tensor formulation for a single crystal in quadratic form can therefore be written as,

$$\lambda = \frac{3}{2}\lambda_{100}\left(m_1^2\beta_1^2 + m_2^2\beta_2^2 + m_3^2\beta_3^2 - \frac{1}{3}\right) + 3\lambda_{111}(m_1 m_2 \beta_1\beta_2 + m_2 m_3 \beta_2\beta_3 + m_1 m_3 \beta_1\beta_3)[14]$$

Where m is the direction vector and λ the magnetostriction. The magnetostrictive material used in the sensor development was a polycrystalline material [19] without a definite orientation therefore,

$$\lambda_s = \frac{2}{5}\lambda_{100} + \frac{3}{5}\lambda_{111} \quad [15]$$

Equations [14] and [15] were therefore used in COMSOL to formulate magnetostriction and therefore magnetostrictive strain modeled by,

$$\varepsilon_{me} = \frac{3}{2}\frac{1}{M_s^2}\left[\lambda_{100}\mathrm{dev}(M \otimes M) + (\lambda_{111} - \lambda_{100})\sum_{i\neq j} M_i M_j (e_i \otimes e_j)\right] \quad [16]$$

The strain components in this work consisted of unequal strain fields but similar properties at saturation. Strains within the magnetostrictive sensor composite could be related to magnetization by[19],

$$\varepsilon = s_H S - d_{HT}^T H \quad [17]$$

Where ε is the strain, S the stress applied, H the magnetic field, d_{HT} the piezomagnetic coupling matrix and s_H the compliance matrix. The magnetic flux density can therefore be written as,

$$B = d_{HT} S + \mu_0 \mu_{rT} H \quad [19]$$

Where μ_0 represents the magnetic permeability and μ_{rT} the relative magnetic permeability at constant stress. Therefore, the formulation of the linear response around a given bias state defined by a pre-magnetization vector M_0 is given by[19],

$$M = M_0 + M_1 = [M_{0,1}, M_{0,2}, M_{0,3}] + M_1 \quad [18]$$

Given that M_1 is a perturbation and the strains are in form,

$$\varepsilon_{me} = \frac{\lambda_s}{M_s^2}\begin{bmatrix} 2M_{0.1} & -M_{0.2} & -M_{0.3} \\ -M_{0.1} & 2M_{0.2} & -M_{0.3} \\ -M_{0.1} & -M_{0.2} & 2M_{0.3} \\ 0 & 3M_{0.3} & 3M_{0.2} \\ 3M_{0.3} & 0 & 3M_{0.1} \\ 3M_{0.2} & 3M_{0.1} & 0 \end{bmatrix} \quad [19]$$

The magnetostrictive strains were in the presence of a magnetic field and the nonlinear implicit relation used to determine the nonlinear magnetization is given as,

$$M = M_s L(|H_{eff}|)\frac{H_{eff}}{|H_{eff}|} \quad [20]$$

Where the Langevin function L[27] [19] is,

$$L = \coth\left(\frac{3\chi_m|H_{eff}|}{M_s}\right) - \frac{M_s}{3\chi_m|H_{eff}|} \quad [21]$$

Where magnetic susceptibility in the initial linear region is χ_m. The model variation beyond saturation magnetostriction affected the stability of the sensor response. For cubic crystals, the contribution of mechanical stresses to the effective magnetic field and magnetization is therefore formulated within[19],

$$H_{eff} = H + \frac{3}{\mu_0 M_s^2}\left[\lambda_{100}S_{ed} + (\lambda_{111} - \lambda_{100})\sum_{i\neq j}(S_{ed})_{ij}(e_i \otimes e_j)\right]M \quad [22]$$

The Villari effect was therefore used to monitor the deviatoric strains within a composite sample applying strains to the magnetostrictive material. A copper planar coil detected the variation in magnetization around the sensor. The physics-controlled mesh was enabled in the model physics to achieve a clean mesh for the coils. Even though the composite plies in this work were in one direction, Helmholtz free energy function [28] was proposed to define the finite strains of the fiber

reinforced polymer composites. This depended on the composite fiber directions and the deformation gradient. A Stationary solver was used in this work and depiction of the magnetic flux density around magnetostrictive sensor within the composite.

The flow of electrical current through the excitation coil created an electrical field contributing the excitation of the magnetostrictive sensor. Villari effect of the magnetostrictive material was in the presence of a magnetic field. The increase in magnetic field intensity within the COMSOL model reflected in the change in magnetic flux density which decreased to the remanence point. To understand the interaction of the electrical field with a composite damped magnetostrictive material, the change in magnetic field around the magnetostrictive material was studied as shown

i

5.3 Discussion

FEA numerical experiments illustrated a more stable output for the magnetostrictive sensor designed in this work. The displacement was proportional to the applied stress. The composite was loaded in the principal axes corresponding the elastic constants. These are defined as E22 transverse elastic moduli, E11 parallel elastic moduli and the shear modulus G12 as Figure 37. The presence of a sensor material within the composite contributed to the centered strains around edges of the Terfenol-D material. These stress distributions are shown in Figure 37, showing the initial stress distribution around the sensor before loading and the development of focused stresses around the sensor as the composite is loaded.

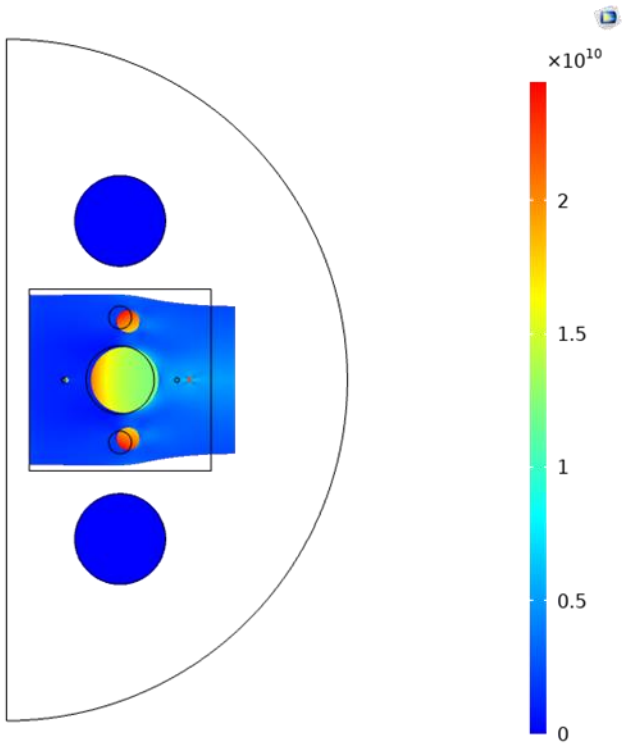

Figure 37. Shows the initial stress distribution (×10^10 Pa) around the sensor as the composite is loaded.

The fractional change in length of the composite sample embedded with magnetostrictive sensor which is the overall strain was determined using the displacements during loading using the equation below.

$$\varepsilon_x = \frac{\left(u+\frac{\partial u}{\partial x}\cdot dx\right)-u}{dx} = \frac{\partial u}{\partial x} \qquad [2]$$

The presence of the magnetostrictive powdered material within the composite varied the strain response of the composite. To further verify the initial COMSOL results, a finer mesh resolution was applied to find a more accurate solution. Computational time increased but a similar trend in sensor response was observed. This system entailed electrical fields from the excitation coil to the magnetostrictive sensors in the presence of a magnetic field. Maxwell equations partial differentials play a vital role in this study for the coupling of magnetic properties with the electrical

properties. COMSOL Multiphysics solver using the system's input data showed the highest magnetic flux density of 2.14 e-8 T as shown in Figure 38. The pickup coil was able to detect the change in magnetic field as tensile load is applied to the composite. The interaction of the composite material with the magnetic, electrical and magnetostrictive properties contributed to the magnetization around the sensor. The contribution of Terfenol-D volumetric fraction on the overall Villari effect was determined by the variation of powdered particles size. Terfenol-D particles of sizes of 100μm, 150μm and 230μm were modeled in this work having volumetric fraction contributions of 0.025%, 0.04% and 0.06% respectively. This contributed to the change in magnetic field around the sensor area as load is applied.

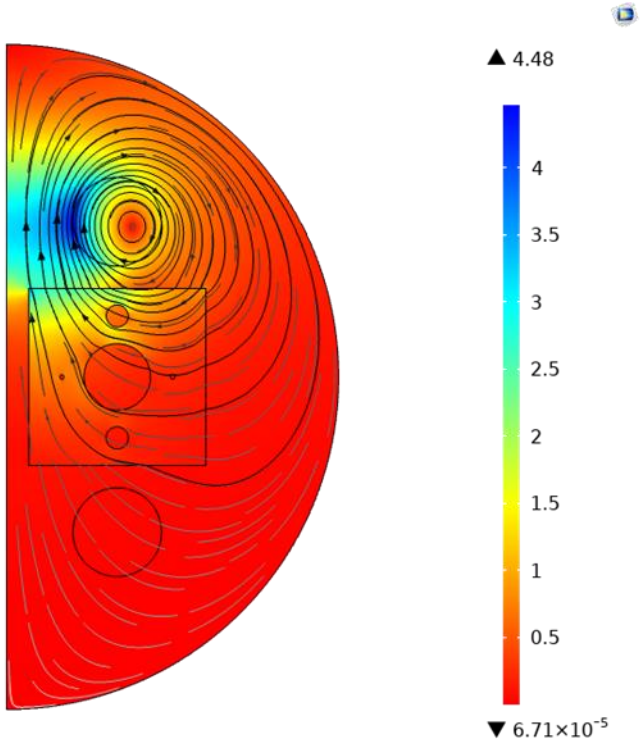

Figure 38. COMSOL model loading and sensor response magnetic flux density (T) a) magnetostrictive sensor magnetic field change.

The change in particle size also contributed to the resistance of the magnetostrictive material change to magnetization. This increased the magnetostrictive material susceptibility to change in magnetization as shown in Figure 38. Coercivity decrease was observed with increase in size of the Terfenol-d particles. The sensor response proportionality to loading was due to the elimination of fabrication defects from experimental tests.

5.4 Conclusion

A COMSOL model for a fiber reinforced composite embedded with Terfenol-D nanomaterial is developed. This model includes a sensor detection system used for both excitation and sensor response recognition. For modeling magnetostrictive material properties with the composite, linear coupled magnetostrictive equations in terms of stress, strain, magnetic field, magnetic flux density, and constant material properties were coupled with solid mechanics physics. From this model, parameters such as stresses, strains, sensor voltage change, and magnetic flux variations were obtained. The data acquired from this model was compared with experimental data. Both tensile and dynamic fatigue tests were part of the experimental work. COMSOL model proved to have a higher sensor sensitivity as compared to that from carbon fiber reinforced composites and testing glass fiber reinforced polymer composites. Higher voltage changes were displayed in the COMSOL model while experimental test samples failed at lower strains therefore limiting sensor voltage response to Villari effect. Future work will include advanced fabrication methods for composite samples and variations of sensor material weight fraction within the composite.

5.5 References

[1] S. Gholizadeh, “A review of non-destructive testing methods of composite materials,” in Procedia Structural Integrity, 2016, vol. 1, pp. 50–57.

[2] M. Kuhnt, M. Marsilius, T. Strache, C. Polak, and G. Herzer, “Magnetostriction of nanocrystalline (Fe,Co)-Si-B-P-Cu alloys,” Scr. Mater., vol. 130, pp. 46–48, Mar. 2017.

[3] M. Kachniarz, A. Bieńkowski, J. Salach, and R. Szewczyk, “Magnetoelastic Villari Effect in Ferrite Materials for Force and Stress Sensors Working in Low Magnetizing Field Region,” vol. 133, 2018.

[4] R. G. QHOBOSHEANE et al., “Design of Embedded Wireless Sensors for Real-Time and In-Situ Strain Sensing of Fiber Reinforced Composites,” Struct. Heal. Monit. 2019, vol. 0, no. 0, 2019.

[5] I. P. Sfikas, J. Ingham, and J. Baber, “Simulating thermal behaviour of concrete by FEA: state-of-the-art review,” Proc. Inst. Civ. Eng. - Constr. Mater., vol. 171, no. 2, pp. 59–71, Apr. 2018.

[6] P. Basu, “Gasification Theory and Modeling of Gasifiers,” in Biomass Gasification Design Handbook, Elsevier, 2010, pp. 117–165.

[7] G. N. Weisensel, R. L. Zrostlik, and G. P. Carman, “Advanced magnetostrictive finite element method (FEM) modeling development,” 1999, p. 110.

[8] F. C. Graham, C. Mudivarthi, S. Datta, and A. B. Flatau, “Modeling of a Galfenol transducer using the bidirectionally coupled magnetoelastic model,” Smart Mater. Struct., vol. 18, no. 10, 2009.

[9] S. Hussain and D. A. Lowther, “An Efficient Implementation of the Classical Preisach Model.”

[10] “COMSOL Multiphysics® Modeling Software.” [Online]. Available: https://www.comsol.com/. [Accessed: 05-Mar-2020].

[11] S. Zhou, T. Rabczuk, and X. Zhuang, “Phase field modeling of quasi-static and dynamic crack propagation: COMSOL implementation and case studies,” Adv. Eng. Softw., vol. 122, pp. 31–49, Aug. 2018.

[12] V. Antonucci, M. Esposito, R. Marzella, M. Giordano, P. Le, and E. Fermi, “Numerical and Experimental Study of a Concentrated Indentation Force on Polymer Matrix Composites Imast-Technological District on Polymeric and Composite Engineering Structures.”

[13] R. Carbone and A. Langella, “Numerical Modeling of Resistance Welding Process in Joining of Thermoplastic Composite Materials Using Comsol Multiphysics.”

[14] T. Y. Sun, L. Sun, Z. H. Yong, H. L. W. Chan, and Y. Wang, “Estimation of the magnetoelectric coefficient of a piezoelectric- magnetostrictive composite via finite element analysis,” in Journal of Applied Physics, 2013, vol. 114, no. 2, p. 027012.

[15] E. Silberberg, “The le chatelier principle as a corollary to a generalized envelope theorem,” J. Econ. Theory, vol. 3, no. 2, pp. 146–155, 1971.

[16] M. Altin Karataş and H. Gökkaya, “A review on machinability of carbon fiber reinforced polymer (CFRP) and glass fiber reinforced polymer (GFRP) composite materials,” Defence Technology, vol. 14, no. 4. China Ordnance Society, pp. 318–326, 01-Aug-2018.

[17] R. Brito-Pereira, C. Ribeiro, S. Lanceros-Mendez, and P. Martins, “Magnetoelectric

response on Terfenol-D/ P(VDF-TrFE) two-phase composites," Compos. Part B Eng., vol. 120, pp. 97–102, Jul. 2017.

[18] "Structural Mechanics MODULE V E R S I O N 3. 4 MODEL LIBRARY COMSOL Multiphysics," 1994.

[19] Comsol, "The Structural Mechanics Module User's Guide," 2018.

[20] J. Slak and G. Kosec, "Adaptive Radial Basis Function-generated Finite Differences method for contact problems."

[21] S. Minera, M. Patni, E. Carrera, M. Petrolo, P. M. Weaver, and A. Pirrera, "Three-dimensional stress analysis for beam-like structures using Serendipity Lagrange shape functions," Int. J. Solids Struct., vol. 141–142, pp. 279–296, Jun. 2018.

[22] W. Huang, Z. Deng, M. J. Dapino, L. Weng, and B. Wang, "Electromagnetic-mechanical-thermal fully coupled model for Terfenol-D devices," J. Appl. Phys., vol. 117, no. 17, p. 17A915, May 2015.

[23] "AC/DC Module User's Guide," 1998.

[24] M. Kumar, S. Kumar, and S. Santapuri, "Computationally efficient modeling of magnetostrictive material based actuator devices."

[25] G. Riesgo et al., "Villari effect in silicone/FeGa composites," Bull. Mater. Sci., vol. 42, no. 5, pp. 1–7, Oct. 2019.

[26] Z. Xu, P. Li, and J. Tang, "Simulation analysis of magnetic field of degaussing coils by COMSOL," 2020, pp. 3537–3542.

[27] S. Steentjes, M. Petrun, G. Glehn, D. Dolinar, and K. Hameyer, "Suitability of the double Langevin function for description of anhysteretic magnetization curves in NO and GO electrical steel grades," AIP Adv., vol. 7, no. 5, p. 056013, May 2017.

[28] G. A. Holzapfel, Nonlinear solid mechanics : a continuum approach for engineering. Wiley, 2000.

[29] C. Martin and D. A. H. G. & O. I. Berg, "Naval Ordnance Laboratory (NSWC White Oak)," NR-Eligibility Form, 1997.

[30] M. J. Dapino, R. C. Smith, F. T. Calkins, and A. B. Flatau, "A MAGNETOELASTIC MODEL FOR VILLARI-EFFECT MAGNETOSTRICTIVE SENSORS."

[31] S. Islam et al., "Structural Health Monitoring of Fiber-Reinforced Composite Using Wireless Magnetostrictive Sensors," in SAMPE 2019 - Charlotte, NC, 2019.

[32] "Lock In Amplifier - SR860." [Online]. Available: https://www.thinksrs.com/products/sr860.html. [Accessed: 05-Mar-2020].

[33] A. Joseph, D. Vasanthi, and M. John, "Low Cost Embedded Design for Wireless Remote Monitoring of Measurement Data in LabVIEW," in 2018 International Conference on Circuits and Systems in Digital Enterprise Technology, ICCSDET 2018, 2018.

Chapter 6: Conclusion

This work shows the development of a smart self-sensing composite. The composite piezoelectric property is achieved from the dispersion of single-walled carbon nanotubes, and the magnetostrictive property is achieved from Terfenol-D nanoparticle dispersion in the interior of the laminate.

A finite element analysis (FEA) study was conducted to study the mechanical, electrical and magnetic behavior of this composite to characterize its piezoelectric and magnetostrictive self-sensing responses in the presence of applied stress. The electric polarization of the piezoelectric material was found to increase rapidly with increase in strain. High piezoelectric responses were observed at sections of the composites with the highest change in length. The COMSOL Multiphysics® magnetostrictive response was characterized by studying the change in magnetic field around the composite sample. The strain change in the composite sample resulted in a higher magnetization of the composite sample. This increase in magnetization is related to the solid mechanics properties of the material following the Villari effect (i.e., the change in the magnetic susceptibility of a material when subjected to a mechanical stress), therefore showing composite sensitivity to strains.

Experimental tensile tests of composite samples without any particles, samples with SWCNTs, samples with Terfenol-D nanoparticles and samples with both SWCNTs and Terfenol-D nanoparticles were conducted. It was observed that increase in Terfenol-D nanoparticles volume fraction increases the change in magnetization and, therefore, voltage response up to the point of saturation. The optimum change in amplitude was observed at 0.20% volume

fraction of Terfenol-D nanoparticles. A constant ratio of SWCNTs was maintained, and maximum change in electrical resistance was at 7.4%.

Fracture toughness for the samples with all nanoparticles was explored, and the results showed improved resistance to crack propagation. This is due to the presence of SWCNTs and, therefore, proved that the mechanical properties affected by the presence of Terfenol-D alloys in the composites can be offset by the dispersion of SWCNTs and still maintain the self-sensing property of the composite.